

1 **Material aging causes centrosome weakening and disassembly**
2 **during mitotic exit**

3
4 Matthäus Mittasch^{1,3}, Vanna M. Tran^{2,3}, Manolo U. Rios², Anatol W. Fritsch¹, Stephen J.
5 Enos¹, Beatriz Ferreira Gomes¹, Alec Bond², Moritz Kreysing^{1,4}, Jeffrey B. Woodruff^{2,4}

6
7 1. Max Planck Institute of Molecular Cell Biology and Genetics, Pfotenstrasse 108, 01307
8 Dresden, Germany

9 2. Dept. of Cell Biology, Dept. of Biophysics, UT Southwestern Medical Center, Dallas, TX 75390,
10 USA

11 3. These authors contributed equally

12 4. For correspondence: kreysing@mpi-cbg.de, jeffrey.woodruff@utsouthwestern.edu

13
14 **ABSTRACT**

15 Centrosomes must resist microtubule-mediated forces for mitotic chromosome
16 segregation. During mitotic exit, however, centrosomes are deformed and fractured by
17 those same forces, which is a key step in centrosome disassembly. How the functional
18 material properties of centrosomes change throughout the cell cycle, and how they are
19 molecularly tuned remain unknown. Here, we used optically-induced flow perturbations
20 to determine the molecular basis of centrosome strength and ductility in *C.*
21 *elegans* embryos. We found that both properties declined sharply at anaphase onset,
22 long before natural disassembly. This mechanical transition required PP2A phosphatase
23 and correlated with inactivation of PLK-1 (Polo Kinase) and SPD-2 (Cep192). *In vitro*,
24 PLK-1 and SPD-2 directly protected centrosome scaffolds from force-induced
25 disassembly. Our results suggest that, prior to anaphase, PLK-1 and SPD-2 confer
26 strength and ductility to the centrosome scaffold so that it can resist microtubule-pulling
27 forces. In anaphase, centrosomes lose PLK-1 and SPD-2 and transition to a weak, brittle
28 state that enables force-mediated centrosome disassembly.

30 **INTRODUCTION**

31

32 Centrosomes nucleate and anchor microtubules that comprise the mitotic spindle, which
33 segregates chromosomes during somatic cell division. Centrosomes are micron-scale,
34 membrane-less organelles containing a structured centriole pair surrounded by an
35 amorphous protein mass called pericentriolar material (PCM). PCM carries out most of
36 the functions of a centrosome, including directing cell polarity, cell migration, and
37 chromosomal segregation (Conduit et al., 2015; Woodruff et al., 2014)

38

39 For chromosome segregation, centrosomes must bear microtubule-dependent loads that
40 create tensile stresses. Motor proteins anchored at the plasma membrane attach to and
41 walk along astral microtubules extending from centrosomes. These spatially-fixed motors
42 thus generate cortically-directed pulling forces on centrosomes, and the balance of those
43 forces determines the ultimate position of the mitotic spindle (Colombo et al., 2003;
44 Gonczy et al., 2001; Grill et al., 2001; McNally, 2013; Nguyen-Ngoc et al., 2007). During
45 this time, centrosomes maintain a compact, spherical shape. However, once
46 chromosome segregation is complete and the cell exits mitosis, centrosomes are
47 deformed and fractured by the same microtubule-mediated forces, which is a pronounced
48 event during centrosome disassembly (Megraw et al., 2002; Severson and Bowerman,
49 2003). How the cell regulates the structural and material integrity of centrosomes is
50 unclear. One possibility is that an increase in cortical forces during mitotic exit induces
51 centrosome disassembly. In *C. elegans* embryos, the magnitude of microtubule-mediated
52 pulling forces does increase during the metaphase-anaphase transition. Yet, the same
53 increase in pulling forces also occurs in metaphase-arrested embryos without leading to
54 centrosome deformation or fracture (Labbe et al., 2004). Furthermore, artificially
55 increasing pulling forces via *csnk-1* RNAi does not cause premature centrosome
56 disassembly (Magescas et al., 2019; Panbianco et al., 2008). These studies suggest that
57 induction of centrosome deformation and fracture during mitotic exit cannot be sufficiently
58 explained by increased microtubule-mediated forces. An alternative hypothesis is that
59 centrosome mechanical properties significantly change to permit force-driven fracture
60 and dispersal during mitotic exit.

61 PCM provides most of the mass and microtubule nucleation capacity of a centrosome,
62 and it is widely believed to be responsible for bearing microtubule-mediated forces. PCM
63 is dynamic and expands in size and complexity as cells prepare for mitosis. Self-
64 assembly of coiled-coil proteins, such as Cdk5Rap2 (vertebrates), Centrosomin (*D.*
65 *melanogaster*) and SPD-5 (*C. elegans*), creates the underlying structural scaffold of PCM
66 which then recruits “client” proteins that nucleate and regulate microtubules (Conduit et
67 al., 2010; Conduit et al., 2014a; Fong et al., 2008; Hamill et al., 2002; Woodruff et al.,
68 2017; Woodruff et al., 2015). Formation of such micron-scale scaffolds requires additional
69 regulatory clients like Polo Kinase, Aurora A Kinase, and SPD-2/Cep192 (Conduit et al.,
70 2014a; Conduit et al., 2014b; Gomez-Ferreria et al., 2007; Hamill et al., 2002; Hannak et
71 al., 2001; Haren et al., 2009; Lee and Rhee, 2011; Pelletier et al., 2004; Zhu et al., 2008).
72 PCM disassembles at the end of each cell cycle, but the mechanism is not well
73 understood. While this process involves microtubule-mediated PCM fracture and reversal
74 of Polo Kinase phosphorylation (Enos et al., 2018; Magescas et al., 2019; Pimenta-
75 Marques et al., 2016), it remains unclear how PCM fracture is initiated, which key
76 molecular targets are de-phosphorylated, if these activities are linked, and how dynamic
77 material changes might contribute to the disassembly process.

78
79 A material’s load-bearing capacity is determined by its ability to resist permanent
80 deformation and fracture upon stress. In materials science, these properties are
81 described as “strength” and “ductility”, respectively. Strength is achieved through high
82 affinity bonding and serves to maintain the material’s shape but can sometimes sacrifice
83 flexibility. Ductility is achieved through breakage and reformation of sacrificial bonds or
84 localized neighbor exchange, which dissipates energy over time but sacrifices the
85 material’s shape. For example, glass requires large forces to deform, but it cannot deform
86 much before shattering; thus, glass has high strength and low ductility. On the other hand,
87 chewing gum is easily deformed, and it will stretch to great lengths before breaking; thus,
88 gum has low strength and high ductility. Materials with the highest load-bearing capacity
89 are those that combine strength and ductility, such as rubbers, polyampholyte gels, and
90 high-entropy alloys (George et al., 2019; Sun et al., 2013). Over time, these properties

91 can change via chemical or physical modifications, which is referred to as “material
92 aging”.

93

94 For the centrosome, it remains unexplored how molecular-level interactions between
95 PCM proteins generate meso-level mechanical properties like strength and ductility and
96 how these properties change with time. The non-covalent interactions between PCM
97 scaffold proteins, as well as cross-linking of scaffold molecules by PCM clients, could all
98 contribute. In general, characterizing the mechanical properties of living soft matter—such
99 as cells, organelles, and protein assemblies—has been challenging due to their size (sub-
100 micrometer scale) and low abundance (sub-milligram scale). Techniques like atomic
101 force microscopy and optical trapping can be useful in this respect, but they are limited to
102 easily accessible samples, like the outer membrane of cultured cells and reconstituted
103 protein complexes. As a complementary method to actively probe mechanical properties
104 in cells with limited accessibility, we previously used focused light-induced cytoplasmic
105 streaming (FLUCS)(Mittasch et al., 2018). Specifically, we showed how FLUCS can
106 reveal robust power-law-rheology signatures within the cell cytoplasm, to distinguish
107 between fluid and gel-like states. Fluids undergo unconstrained motion proportional to
108 stimulus time (i.e., they flow), while solids and gels undergo only limited deformations,
109 which stall after small amounts of time due to their intrinsic elastic constraints. As FLUCS
110 functions via thermoviscous flows, which develop independent of the absolute viscosity
111 of the fluid (Weinert et al., 2008), FLUCS is particularly suited to distinguish between
112 highly viscous phases and elastic phases. Such a distinction could not be achieved by
113 passive microrheology, as these two states would exhibit the same fingerprint of reduced
114 motion.

115

116 The *C. elegans* embryo is an ideal system to dissect the molecular determinants of PCM
117 load-bearing capacity. First, *C. elegans* has a limited core set of proteins needed for rapid
118 PCM assembly and disassembly, most of which are conserved across eukaryotes: PLK-
119 1 (Polo Kinase homolog), SPD-2 (Cep192 homolog), SPD-5 (functional homolog of
120 Centrosomin and Cdk5Rap2), and LET-92^{SUR-6} (PP2A^{B55 α} phosphatase homolog)
121 (Decker et al., 2011; Enos et al., 2018; Hamill et al., 2002; Kemp et al., 2004; Magescas

122 et al., 2019; Pelletier et al., 2004; Schlaitz et al., 2007). Second, it is possible to
123 reconstitute PCM assembly and microtubule nucleation *in vitro* using purified *C. elegans*
124 proteins (Woodruff et al., 2017; Woodruff et al., 2015). These experiments previously
125 revealed that PCM forms via self-assembly of SPD-5 into spherical, micron-scale
126 scaffolds that recruit PCM client proteins. SPD-2 and PLK-1 enhance SPD-5 self-
127 assembly, while PP2A^{SUR-6} removes PLK-1-derived phosphates and promotes PCM
128 disassembly. However, these experiments did not reveal the mechanical properties of the
129 SPD-5 scaffold nor how they are tuned in a cell-cycle-dependent manner.

130
131 Here, we ask 1) how centrosomes undergo dynamic structural changes to withstand high
132 tensile stresses in mitosis but not during mitotic exit, 2) which mechanical properties are
133 associated with these distinct functional states, and 3) which molecular players and logics
134 regulate the transient existence of centrosomes. To answer these questions, we
135 combined genetics and pharmacological intervention with FLUCS to study the mechanical
136 properties of PCM in *C. elegans* embryos. Our results revealed that PCM transitions from
137 a strong, ductile state in metaphase to a weak, brittle state in anaphase. This mechanical
138 transition is promoted by PP2A^{SUR-6} and opposed by PLK-1 and SPD-2. Our data suggest
139 that mitotic PCM is a composite of a stable SPD-5 scaffold and proteins that dynamically
140 reinforce the scaffold, such as PLK-1 and SPD-2. During spindle assembly, accumulation
141 of PLK-1 and SPD-2 render the PCM tough enough to resist microtubule-pulling forces.
142 During mitotic exit, departure of PLK-1 and SPD-2 weakens the PCM scaffold to allow
143 microtubule-mediated fracture and disassembly. Thus, PCM undergoes cell-cycle-
144 regulated material aging that functions to promote its disassembly.

145
146
147 **RESULTS**
148

149 **FLUCS reveals weakening of the PCM scaffold at anaphase onset in *C. elegans***
150 **embryos**

151 To study the molecular determinants of PCM load-bearing capacity, we studied *C.*
152 *elegans* 1-cell embryos, where growth and disassembly of the PCM scaffold is easily
153 visualized using fluorescently-labeled SPD-5 (mMaple::SPD-5)(Figure 1A). During

154 spindle assembly, the *C. elegans* PCM scaffold is subject to microtubule-mediated pulling
155 forces, but it maintains its spherical shape and structural integrity. However, during
156 telophase, those same pulling forces deform and fracture the PCM scaffold (Figure
157 1A)(Enos et al., 2018; Severson and Bowerman, 2003). We hypothesized that PCM
158 undergoes an intrinsic mechanical transition from a strong, tough state in metaphase to
159 a weak state in telophase.

160

161 We probed PCM mechanical properties using FLUCS-generated flows complemented
162 with fluorescent imaging. Specifically, we equipped a spinning disk confocal microscope
163 with a laser control unit (wavelength = 1455 nm) that creates precise, sub-millisecond
164 thermal manipulations (Figure 1B). Unidirectional scans with this laser at 1500 Hz creates
165 travelling temperature fields that are sufficient to induce flows in a viscous medium,
166 including embryonic cytoplasm (Mittasch et al., 2018)(see Methods). A Peltier-cooled
167 stage insert dissipates excess heat to keep the sample within its physiological
168 temperature range.

169

170 We applied FLUCS to *C. elegans* embryos expressing mMaple::SPD-5 and mCherry-
171 labeled histones (mCherry::H2B). For each experiment, we induced flows crossing the
172 cytoplasm and continuing through the middle of a centrosome, which should apply stress
173 to the PCM scaffold orthogonal to microtubule-derived tensile stresses (Figure 1C).
174 Based on previous experiments (Mittasch et al., 2018), we predicted that cytoplasmic
175 shear flows should weaken the PCM by the relative displacement of scaffold proteins and
176 create a virtual “notch” in the flow path. We used three different amplitudes for the
177 scanning infrared laser (25, 32, 40 mW) to generate cytoplasmic flow velocities ranging
178 from 5-20 $\mu\text{m}/\text{min}$ (Figure 1D; Movie S1); these flows scaled quadratically with laser
179 power ($R^2= 0.97$), as one would expect for a predominantly viscous medium (Figure S1A).
180 Simultaneously, we cooled embryos to 17°C, such that the embryo cytoplasm never
181 exceeded 23°C during laser scanning (*C. elegans* embryos develop properly at any
182 temperature between 16°C and 25°C)(Begasse et al., 2015).

183

184 As shown in Figure 1E, FLUCS deformed and fractured mature PCM in anaphase
185 embryos. We also detected a slight increase in cytoplasmic fluorescence surrounding the
186 PCM during FLUCS, indicating that flows can dislodge SPD-5 from the PCM, as predicted
187 (Figure S1B). FLUCS-induced PCM deformation differed starkly between cell cycle
188 stages. FLUCS was not able to visibly deform PCM during metaphase or prior, even
189 though flows were strong enough to detach the centrosome from the spindle and move it
190 toward the cell cortex or out of the focal plane (Figure 1D and S1C and Movies S2, S3;
191 see Metaphase and Prometaphase). On the contrary, FLUCS deformed and eventually
192 fractured PCM during anaphase and telophase (Figure 1E,F; Movie S4,S5); in these
193 experiments, the untreated centrosome remained intact.

194
195 We then quantified 1) the deformation rate, defined by the rate of PCM length change
196 orthogonal to the flow direction, and 2) the fracture probability, defined by the chance that
197 PCM segments detach completely after FLUCS (Figure 1G; see methods). The PCM
198 deformation rate and fracture probability increased with increasing flow velocity and
199 progression through mitosis (Figure 1 H,I). To pinpoint when PCM becomes susceptible
200 to FLUCS-induced deformation, we continuously applied FLUCS to centrosomes starting
201 in metaphase continuing into anaphase. PCM remained spherical and intact during
202 metaphase, but then fractured immediately after anaphase onset, as marked by
203 chromosome segregation (Figure S1D; Movie S6). Our results suggest that PCM
204 resistance to deformation and fracture is high during metaphase, then declines at
205 anaphase onset, ~150s prior to full PCM disassembly in telophase. We refer to this
206 change in PCM mechanical properties hereon as the “PCM weakening transition”.

207
208 Since the generation of FLUCS is accompanied by local temperature gradients, we tested
209 if temperature alone affects PCM structure. Bidirectional scanning at 10 kHz creates local
210 temperature gradients without flow, and these conditions did not cause significant PCM
211 deformation or fracture (Figure 1H,I and S1E). Thus, centrosome perturbation during
212 FLUCS is primarily due to the flows and not temperature gradients *per se*. Furthermore,
213 embryos developed properly after cessation of FLUCS (Figure S1F)(Mittasch et al.,

214 2018). We conclude that this established method can be used to study organelles inside
215 a living cell.

216

217 **PCM weakens in anaphase independent of cortical force generation**

218 We next wondered if our FLUCS results could be explained by cell-cycle-dependent
219 changes in PCM mechanical properties or changes in cortical force generation. During
220 the metaphase-anaphase transition in early *C. elegans* embryos, cortical pulling forces
221 increase to induce transverse oscillations and posterior positioning of the mitotic spindle
222 (Pecreaux et al., 2006). Depleting the proteins GPR-1 and GPR-2 (*gpr-1/2(RNAi)*)
223 significantly reduces cortical microtubule-pulling forces and prevents spindle
224 displacement, spindle oscillation, and PCM deformation and fracture (Colombo et al.,
225 2003; Enos et al., 2018; Grill et al., 2003; Magescas et al., 2019; Pecreaux et al., 2006).
226 Thus, we performed FLUCS in *gpr-1/2(RNAi)* embryos, where we expect only residual
227 cortical forces that remain relatively constant throughout mitosis.

228

229 In both wild-type and *gpr-1/2(RNAi)* embryos, FLUCS deformed PCM in anaphase and
230 telophase, but not in metaphase. However, in *gpr-1/2(RNAi)* embryos, FLUCS-induced
231 PCM deformation rates were slower (Figure 2 A,B; Figure S2A), and FLUCS caused
232 fracturing only in telophase (Figure 2C). These results suggest that PCM mechanical
233 properties change during mitotic exit, but that cortical pulling forces are required to
234 disperse and fracture the pre-weakened PCM scaffold. To further test this idea, we
235 applied 10 µg/ml nocodazole to depolymerize microtubules and performed high-flow
236 FLUCS. Under these conditions, FLUCS did not visibly affect PCM during metaphase,
237 but did dislodge SPD-5 protein from the PCM during telophase (Figure 2D); we did not
238 observe stretching or clean fracture of the PCM during any cell cycle stage. These results
239 indicate that 1) the interactions between SPD-5 scaffold molecules weaken independent
240 of microtubule-pulling forces during mitotic exit, and 2) microtubule-pulling forces are
241 required for stretching and fracture of the PCM during mitotic exit. To test if microtubule-
242 mediated pulling forces could be sufficient to deform PCM already in metaphase, we
243 depleted a negative regulator of GPR-1/2, casein kinase 1 gamma (*csnk-1(RNAi)*), which
244 is reported to increase cortical pulling forces ~1.5-fold (Panbianco et al., 2008). We did

245 not observe premature deformation or fracture of PCM under these conditions, even
246 though the spindle rocked violently in metaphase (Figure S2B). We conclude that an
247 intrinsic mechanical change in the SPD-5 scaffold is the main driver of PCM weakening
248 during anaphase entry.

249
250 We next examined the viscoelastic properties of PCM during anaphase by measuring the
251 time-dependent deformation of PCM during FLUCS and relaxation after FLUCS was
252 turned off. We used *gpr-1/2(RNAi)* embryos to allow residual pulling forces but prevent
253 spindle oscillations, which could complicate our analysis. We observed that continuous
254 application of medium and high-flow FLUCS in *gpr-1/2(RNAi)* embryos caused time-
255 dependent strain of the PCM scaffold (Figure 2E). Thus, anaphase PCM is ductile and
256 can experience micron-scale structural rearrangements without complete fracture during
257 stress. Such behavior is seen in viscous materials. When we turned off FLUCS, PCM
258 remained in its strained, elongated state, indicating the absence of a dominant elastic
259 element strong enough to return the PCM to its original shape (Figure 2 E,F).

260
261 Overall, our FLUCS experiments suggest that the PCM structurally weakens after
262 metaphase. This weakening transition would presumably facilitate PCM disassembly by
263 enabling microtubule-dependent pulling forces to fracture and disperse the PCM scaffold
264 in telophase.

265
266 **PCM undergoes stepwise compositional changes following anaphase onset**
267 We next investigated the molecular mechanism underlying the PCM weakening transition,
268 in particular, identifying the specific players that determine the dynamic regulation of PCM
269 strength and ductility. PCM is a heterogeneous assembly of proteins required for its
270 assembly and function (Figure 3A). In particular, two critical regulatory proteins, PLK-1
271 (Polo-like Kinase) and SPD-2 (Cep192 homolog), interact with the scaffold protein SPD-
272 5 and enhance its self-assembly into supramolecular structures (Cabral et al., 2019;
273 Decker et al., 2011; Woodruff et al., 2017; Woodruff et al., 2015). PLK-1 and SPD-2, as
274 well as other PCM-localized client proteins, might also reinforce the mature SPD-5

275 scaffold. On the other hand, loss or inactivation of these proteins could weaken the PCM
276 scaffold.

277
278 To analyze PCM composition changes during anaphase, we visualized 9 different GFP-
279 labeled PCM proteins relative to a standard PCM marker, mCherry:: γ -tubulin. We then
280 measured the integrated density of PCM-localized mCherry and GFP signals during
281 mitosis (Figure 3B). The curves in Figure 3D and Figure S3 represent averages for >10
282 experiments (mean +/- 95% CI). mCherry:: γ -tubulin signal peaked ~75-100s after
283 anaphase onset, then declined, indicating its departure from PCM. GFP:: γ -tubulin
284 behaved similarly, as expected (Figure 3C,D and Figure S3). PLK-1 signal decreased
285 immediately after anaphase onset and was no longer detectable ~100s later. SPD-2 also
286 departed from the PCM prior to γ -tubulin. However, the main scaffold protein SPD-5
287 departed afterward. All other proteins departed coincidentally with γ -tubulin or soon
288 afterward. TPXL-1 and AIR-1 departed in a biphasic manner: an initial loss of signal
289 occurred prior to γ -tubulin departure, then a second phase occurred after γ -tubulin
290 departure. To compare departure kinetics across all experiments, we determined the
291 halfway point of disassembly for each individual GFP and mCherry curve per experiment,
292 then calculated the time differential between halfway points (Δt_{EXIT} ; Figure 3E). The
293 results for anterior and posterior PCM proteins are summarized in Figure 3F and 3G,
294 respectively. A negative Δt_{EXIT} value indicates GFP::PCM protein departure before γ -
295 tubulin, and a positive value indicates departure after γ -tubulin. Our results reveal that
296 PCM composition changes in a stepwise manner during anaphase: PLK-1 departs first,
297 followed by SPD-2, γ -tubulin, TAC-1, and finally SPD-5 and proteins that form tight
298 complexes with SPD-5 (RSA-1, RSA-2). TPXL-1 and AIR-1 were more variable in their
299 departure, possibly because they localize both to PCM and microtubules that remain after
300 disassembly of the PCM scaffold (Hannak et al., 2001; Ozlu et al., 2005).

301
302 **Polo Kinase and SPD-2 reinforce the PCM scaffold by increasing its strength and**
303 **ductility**

304 PLK-1 and SPD-2 are the first proteins to depart the PCM during anaphase, when the
305 PCM begins to weaken. Thus, we hypothesized that PLK-1 and SPD-2 normally reinforce

306 the PCM to achieve full strength and stability in metaphase. If this idea is correct, then
307 acute inhibition of PLK-1 phosphorylation or SPD-2 in metaphase might prematurely
308 weaken the PCM, accelerate its disassembly, or reveal hidden material states not
309 previously visible.

310

311 For acute inhibition of PLK-1, we treated semi-permeable embryos (via *perm-1(RNAi)*)
312 with 10 μ M Polo Kinase inhibitor BI-2536 in prometaphase (Carvalho et al., 2011). After
313 2 minutes in drug solution, we applied low, medium, and high-flow FLUCS to centrosomes
314 (Figure 4A-C). Under these conditions, low and medium-flow FLUCS deformed
315 metaphase PCM in BI-2536-treated embryos, in contrast to wild-type embryos (Figure
316 4B); in both cases, PCM fracture did not occur. Under high-flow FLUCS, BI2536 treatment
317 increased PCM deformation rate as much as ~11-fold with fracture occurring only in a
318 minority of the cases (30%) (Figure 4A,C). The fact that PLK-1 inhibition enabled PCM to
319 be deformed easily without necessarily fracturing suggests that PLK-1 mostly determines
320 PCM strength. This experiment also reveals that wild-type PCM is ductile during
321 metaphase; this could not be observed previously because the deformation resistance of
322 wild-type PCM was too high. BI-2536 treatment also caused premature disassembly of
323 the SPD-5 scaffold in metaphase-arrested embryos, consistent with previous findings
324 (Figure 4D)(Cabral et al., 2019). Our results show that continuous PLK-1 activity is
325 needed for PCM to achieve full strength and maintain integrity until chromosome are
326 separated.

327

328 Next, we analyzed embryos expressing a temperature-sensitive version of SPD-2 (*spd-*
329 *2(or188ts)*)(Kemp et al., 2004). We mounted *spd-2(or188ts)* *gfp::spd-5* embryos in cold
330 media and maintained the sample at 17°C while imaging until prometaphase, then
331 upshifted the embryos to 25°C for 1 min to inactivate SPD-2^{or188ts}. We then lowered the
332 temperature to 17°C to perform FLUCS in metaphase as per usual (Figure 4E)(Note:
333 because of the local heating caused by FLUCS, the treated centrosome remained at
334 ~23°C throughout the experiments). The absence of fully functional SPD-2 made PCM
335 more susceptible to FLUCS-induced fracture and disintegration at all applied flow
336 velocities (Figure 4E-G). Even in PCM that did not fracture into observable pieces, the

337 GFP::SPD-5 signal decayed after application of FLUCS (Figure 4F). We did not observe
338 this phenotype in wild-type PCM or *spd-2* mutant PCM not treated with FLUCS (Figure
339 4F). Our interpretation of this data is that SPD-2 is required for PCM ductility and strength.
340 Without SPD-2, PCM becomes brittle and susceptible to fracture and diffusion-driven
341 departure of constituents after modest mechanical agitation. In line with this view,
342 inactivation of SPD-2 caused premature disassembly of the SPD-5 scaffold in early
343 anaphase, even without FLUCS perturbations (Figure 4H). Deformation rates were
344 difficult to measure because rapid fracture and vanishing GFP::SPD-5 signal precluded
345 a flow analysis. We conclude that both Polo Kinase and SPD-2 help PCM achieve
346 maximal strength and ductility to prevent disassembly.

347
348 We next used a minimal *in vitro* system to test if PLK-1 and SPD-2 directly affect the
349 mechanical properties of the SPD-5 scaffold. When incubated in a crowded environment
350 (e.g. >4% PEG), purified recombinant SPD-5 assembles into micron-scale condensates
351 that recruit PLK-1, SPD-2, and other PCM proteins (Woodruff et al., 2017). We could not
352 assess SPD-5 condensates using FLUCS because the condensates were propelled
353 quickly away from the flow path (data not shown); thus, our simplified *in vitro* conditions
354 do not exactly match those found in native cytoplasm. As another way to assess the
355 strength of SPD-5 interactions, we induced disassembly of young RFP-labeled SPD-5
356 condensates (500 nM SPD-5::RFP; 5 min after formation) through application of pipetting
357 shear forces and dilution, then measured the amount of condensates that survived using
358 fluorescence microscopy (Figure 5A)(note: dilution is required to prevent SPD-5 re-
359 assembly; thus, this assay tests resistance to disassembly only)(Enos et al., 2018). This
360 treatment completely disassembled condensates composed solely of SPD-5 (Figure
361 5B,C). Addition of constitutively active PLK-1 (PLK-1^{CA}; T194D T-loop phospho-mimic) or
362 SPD-2 prevented SPD-5 condensate disassembly, with the combination of the two
363 yielding the greatest protection (Figure 5B,C). Kinase-dead PLK-1 (PLK-1^{KD}; K67M
364 mutant) did not promote SPD-5 condensate survival. These results suggest that PLK-1
365 phosphorylation of SPD-5, along with direct binding of SPD-2, reinforce the interactions
366 between SPD-5 molecules and thus enhance the ability of PCM to resist disassembly.

367 Our *in vitro* and *in vivo* data together suggest that PLK-1 and SPD-2 tune PCM load-
368 bearing capacity by conferring strength and ductility to the SPD-5 scaffold.

369

370 **Phosphatase PP2A^{SUR-6} promotes PCM disassembly by compromising scaffold
371 ductility**

372 We next investigated how embryos promote the PCM weakening transition during
373 anaphase. PP2A phosphatase localizes to the PCM and plays multiple roles in centriole
374 biogenesis, spindle assembly, and mitotic exit (Wlodarchak and Xing, 2016). The *C.*
375 *elegans* homolog of PP2A (LET-92) complexed with the B55 α regulatory subunit SUR-6
376 (PP2A^{SUR-6}) is required for complete PCM disassembly (Enos et al., 2018; Magescas et
377 al., 2019). We thus tested if PP2A^{SUR-6} drives PCM disassembly by compromising the
378 mechanical properties of PCM.

379

380 We treated semi-permeable one-cell embryos with 10 μ M PP2A inhibitor (LB-100) in
381 metaphase, then performed high-flow FLUCS in anaphase. Unlike in wild-type embryos,
382 where PCM fractured quickly after high-flow FLUCS, the PCM in LB-100-treated embryos
383 stretched orthogonal to the induced flow but resisted fracture (Figure 6A). PCM
384 deformation velocity was ~2-fold higher (0.26 vs. 0.12 μ m/min), initially suggesting that
385 PCM is easier to deform when PP2A is inhibited (Figure 6B). However, PP2A inhibition
386 also elevated the ductility of PCM 1.5-fold (final length divided by the original length) and
387 lowered the fracture probability >2-fold in all cell cycle stages (Figure 6C-D). In 2/10
388 anaphase embryos treated with LB-100, PCM stretched as much as 4-fold in length after
389 FLUCS, reaching up to 10 μ m while staying connected. PCM was also more resistant to
390 fracture in embryos depleted of the PP2A regulatory subunit SUR-6 (Figure S4A-C).
391 These results suggest that, when PP2A is inhibited, the ductile nature of PCM is
392 preserved throughout anaphase, allowing PCM to absorb more energy overall without
393 fracturing. This is likely achieved through “self-healing”, or the breakage and reformation
394 of weak inter-scaffold interactions. The increase in deformation velocity may then result
395 from ductile PCM becoming easier to stretch as it becomes more extended. On the other
396 hand, wild-type PCM is brittle during anaphase and can only be extended short distances
397 before fracturing. We conclude that PP2A normally functions to eliminate “self-healing”

398 PCM scaffold interactions, thus making PCM brittle during anaphase and susceptible to
399 microtubule-mediated fracture in telophase. Consistent with this conclusion, LB-100
400 inhibition of PP2A or depletion of its regulatory subunit SUR-6 inhibited SPD-5 scaffold
401 disassembly in telophase (Figure 6E) (Enos et al., 2018). We speculate that PCM may
402 be less porous in this mutant ductile state compared to the wild-type brittle state, which
403 could delay PCM disassembly further by preventing access of additional disassembly
404 machinery and/or delaying the departure of PLK-1 and SPD-2. Consistent with the latter
405 concept, both *let-92* RNAi and *sur-6* RNAi impaired SPD-2 and PLK-1 departure from
406 PCM during anaphase (Figure S4D-G) (Magescas et al., 2019).

407
408 To determine when and where PP2A might dephosphorylate PCM proteins, we visualized
409 embryos expressing GFP::LET-92, the PP2A catalytic subunit in *C. elegans* (Schlaitz et
410 al., 2007). GFP::LET-92 localized to the PCM and persisted there until SPD-5 scaffold
411 disassembly, approximately 100s after PLK-1 had departed from the PCM (Figure 6F),
412 consistent with previous observations (Magescas et al., 2019). Our results suggest that,
413 during anaphase, Polo Kinase activity at the PCM ceases and PP2A removes Polo-
414 delivered phosphates and contributes to SPD-2 departure. This shift in the balance of
415 phosphorylation and dephosphorylation changes the mechanical properties of the PCM,
416 making it more brittle and susceptible to fracture and dissolution.

417
418 **DISCUSSION**
419 Mitotic spindle assembly and positioning require that centrosomes bear tensile
420 microtubule-dependent forces without structural failure. As mitosis ends, however, these
421 same forces are sufficient to deform and fracture centrosomes, facilitating their
422 disassembly. Disassembly is essential to release centrioles and avoid accumulation of
423 old centrosomes over successive rounds of cell division. Here, we combined flow-driven
424 mechanical perturbations *in vivo* with biochemical reconstitution *in vitro* to determine the
425 molecular mechanisms regulating deformation resistance and fracture resistance of
426 PCM, the outer and most massive layer of a centrosome.

427

428 **PCM mechanical properties, function, and renewal can be achieved through**
429 **transient reinforcement of the PCM scaffold**

430 Using *C. elegans* embryos as a model system, we found that PCM deformation
431 resistance, fracture resistance, and composition are tuned in a cell-cycle-dependent
432 manner (Figure 7A,B). During metaphase, PCM resists both microtubule-mediated forces
433 and induced flow perturbations without deforming or fracturing. In this state, PCM is
434 structured as a reinforced composite, comprising a non-dynamic scaffold of SPD-5
435 molecules filled with a dynamic phase of regulatory molecules like SPD-2 and PLK-1,
436 which frequently bind and unbind the scaffold (Figure 7B). During anaphase, PCM loses
437 PLK-1 and SPD-2 and then becomes susceptible to deformation and fracture. During
438 telophase, PCM is at its weakest and is easily fractured and dispersed by microtubule-
439 mediated forces, a hallmark step in the PCM disassembly process.

440

441 Our implementation of flow perturbations *in vivo* using FLUCS reveals how PLK-1, SPD-
442 2, and PP2A contribute to the dynamic mechanical properties of the PCM. We interpret
443 deformation resistance as an indicator of strength and fracture resistance and strain as
444 indicators of ductility. Wild-type metaphase PCM is highly resistant to flow perturbations,
445 but underlying features appear in different mutant states (Figure 7C). When PLK-1 is
446 inhibited, the PCM scaffold is easily deformed by FLUCS and stretches without fracturing.
447 Thus, PLK-1 normally maintains PCM strength. On the other hand, when SPD-2 is
448 inhibited, the PCM scaffold is easily fractured and dissolved by FLUCS but does not
449 stretch. Thus, SPD-2 normally maintains PCM ductility and strength. Elimination of either
450 PLK-1 or SPD-2 causes premature PCM disassembly, suggesting that the combination
451 of strength and ductility is necessary for PCM function and maintenance during spindle
452 assembly in metaphase. In anaphase, wild-type PCM is more easily deformed and
453 fractured by FLUCS. Yet, when PP2A is inhibited, PCM is difficult to fracture by FLUCS
454 and instead stretches up to 4 times its original length, revealing that the high ductility of
455 the PCM, which was established prior to metaphase, is preserved. Thus, PP2A normally
456 functions to drive PCM disassembly by reducing PCM ductility.

457

458 We propose that that the balance of PLK-1, SPD-2, and PP2A activities determine the
459 mechanical properties and assembly/disassembly state of the PCM (Figure 7D). In
460 metaphase, PLK-1 phosphorylation of SPD-5 and direct binding of SPD-2 reinforce the
461 SPD-5 scaffold, conferring strength and ductility. During anaphase, PLK-1 and SPD-2
462 depart from the PCM, while PP2A phosphatase remains and removes PLK-1-derived
463 phosphates. As a result, PCM becomes progressively brittle and weak, allowing
464 microtubule-dependent forces to deform and fracture it in telophase. Since PLK-1 and
465 SPD-2 stabilize the SPD-5 scaffold, but are themselves dynamic, we call this mode of
466 PCM regulation “transient reinforcement”.

467

468 Transient reinforcement of the PCM scaffold, in theory, could enable cell-cycle regulated
469 PCM assembly, function, and renewal. In preparation for mitosis, PCM must rapidly
470 assemble and provide a solid foundation for nucleating and anchoring microtubules. If
471 PCM assembly fails, then mitotic spindle assembly and chromosome segregation is
472 severely impaired (Doxsey et al., 1994; Hamill et al., 2002; Sunkel and Glover, 1988).
473 PLK-1 and SPD-2 thus play dual roles in PCM functionality: 1) catalyzing assembly of the
474 PCM scaffold and 2) strengthening it to withstand microtubule-dependent pulling forces
475 (shown here). While PCM is stable during spindle assembly, PCM disassembles in
476 telophase only to be rebuilt in the next cell cycle. PCM disassembly is essential for entry
477 into various post-mitotic states, including the formation of acentriolar oocytes and heart
478 tissue (Pimenta-Marques et al., 2016; Zebrowski et al., 2015). How might transient
479 reinforcement enable PCM disassembly and renewal? Based on *in vivo* and *in vitro* FRAP
480 data, PLK-1 and SPD-2 are mobile within the PCM, suggesting that they frequently bind
481 and unbind the SPD-5 scaffold (Laos et al., 2015; Woodruff et al., 2017). Either
482 decreasing their association or increasing their dissociation rates with the SPD-5 scaffold
483 would reduce SPD-2 and PLK-1 levels at the PCM. One potential mechanism is through
484 localized ubiquitination and degradation, which controls Polo Kinase levels at
485 centrosomes in human tissue culture cells during anaphase (Lindon and Pines, 2004). It
486 is currently unknown how PCM levels of SPD-2 or its homolog Cep192 are tuned. The
487 completeness and speed of SPD-2 and PLK-1 removal during anaphase is also
488 suggestive of feedback. Thus, the system could be set up such that minor changes to

489 SPD-2 and PLK-1 affinity elicit large, switch-like changes in PCM structure and
490 mechanical properties. Further experiments are needed to define how the other
491 numerous PCM proteins and centriole tethers contribute to PCM mechanical properties.
492 One possible control point is linkage of the SPD-5 scaffold to the centriole via PCMD-1;
493 inactivation of PCMD-1 or laser ablation of centrioles leads to aberrant PCM deformation,
494 presumably because PCM can no longer fully resist microtubule-pulling forces (Cabral et
495 al., 2019; Erpf et al., 2019).

496

497 **PCM mechanical properties in other eukaryotes**

498 The mechanical properties of PCM in other species have yet to be determined. We
499 speculate that our transient reinforcement model for tuning PCM load bearing capacity
500 may be conserved for three reasons. First, diverse eukaryotic species—nematodes,
501 frogs, flies, and human cells—use both Polo Kinase and SPD-2/Cep192 to enhance
502 assembly of the PCM scaffold (Conduit et al., 2014b; Decker et al., 2011; Haren et al.,
503 2009; Joukov et al., 2014; Kemp et al., 2004; Pelletier et al., 2004; Woodruff et al., 2015).
504 Second, PP2A is highly conserved in eukaryotes and is required for mitotic exit in these
505 species (Wlodarchak and Xing, 2016). Third, in *Drosophila* embryos, PCM undergoes
506 cell-cycle-regulated deformation and fracture, termed “flaring”, which appears similar to
507 disassembling PCM in *C. elegans* (Megraw et al., 2002). PCM flares are visible during
508 interphase, cease during metaphase and anaphase, and then escalate during telophase.
509 Flares also require dynamic microtubules. Thus, *Drosophila* PCM flaring may be due to
510 decreasing PCM strength and ductility during telophase, such that PCM can no longer
511 resist microtubule-mediated forces.

512

513 **Parallels between PCM and common soft materials in engineering**

514 The mechanical properties and structure of mature PCM are analogous to common
515 composite materials such as flexible plastics and hydrogels. Most modern plastics
516 comprise cross-linked polymer chains embedded with plasticizers, chemicals that make
517 the plastic more flexible and ductile. Over time, these plasticizers exit by diffusion, making
518 the remaining plastic brittle and weak, which is a form of material aging. The rubber sole
519 on a shoe will crack with age; flexibility of the old sole can be restored by impregnating

520 the rubber with a plasticizer such as silicone. For PCM, the SPD-5 scaffold is most similar
521 to the polymer chains, whereas PLK-1 and SPD-2 could act as plasticizers. Similar to
522 aging rubber losing its plasticizers, our results show that the PCM scaffold becomes brittle
523 and weak during anaphase, coincident with both PLK-1 and SPD-2 leaving the PCM.

524

525 PCM is also similar to physical composites like polyampholyte hydrogels, which exhibit a
526 unique combination of high tensile strength and flexibility. Polyampholyte gels comprise
527 polymers cross-linked with a combination of high- and low-affinity non-covalent bonds.
528 Upon stress, the low-affinity bonds break and dissipate energy, while the high-affinity
529 bonds maintain the overall supramolecular structure. The low affinity bonds then quickly
530 reform, resulting in self-healing that prevents structural fatigue from repeated stresses
531 (Sun et al., 2013). These bonds also make the material more ductile, such that it will
532 undergo plastic deformation instead of fracturing. For PCM, it is possible that PLK-1,
533 SPD-2, and other PCM-resident proteins dissipate stress by unbinding from the PCM
534 scaffold, then re-binding to achieve self-healing. Eliminating these weak interactions
535 would make the PCM weaker and more brittle. This would naturally occur in anaphase as
536 PLK-1 and SPD-2 depart from PCM. This concept could also explain why FLUCS induces
537 PCM fracture and deformation in metaphase when we acutely inhibit PLK-1 and SPD-2.
538 Alternatively, in PP2A-inhibited embryos, PCM is ductile due to the preservation of low
539 affinity, self-healing bonds. Although stronger and more ductile than normal, this mutant
540 PCM still weakens and disassembles in telophase, suggesting that another yet unknown
541 process disrupts the strong interactions between SPD-5 molecules.

542

543 Conclusion

544 This work establishes that PCM, the most substantial layer of the centrosome, transitions
545 from a strong, ductile state in metaphase to a weak, brittle state in telophase. This
546 transition is driven by PP2A phosphatase and inactivation of Polo Kinase and SPD-2/Cep-
547 192, which are essential for centrosome assembly and reinforce the PCM scaffold during
548 metaphase. This mode of mechanical regulation, which we term “transient reinforcement”,
549 is a functional form of material aging that allows PCM to resist microtubule-mediated
550 tensile stresses during spindle assembly and then to be fractured and disassembled by

551 similar forces during mitotic exit. Implicitly, our work demonstrates how flow perturbations
552 can reveal functional mechanical states of membrane-less organelles in vivo.

553
554
555

FUNDING

556 J.B.W. is supported by a Cancer Prevention Research Institute of Texas (CPRIT) grant
557 (RR170063) and the Endowed Scholars program at UT Southwestern. M.K. is supported
558 by the Max Planck Society and ERC grant 853619, and we acknowledge a DFG-financed
559 DIPP fellowship for M.M.

560

561 ACKNOWLEDGEMENTS

562 We would like to thank Karen Oegema, Arshad Desai, Anthony Hyman, and Bruce
563 Bowerman for providing strains; Andrea Zinke, Anne Schwager, and Susanne Ernst for
564 help with worm maintenance; Carsten Hoege and David Drechsel for providing the
565 CRISPR reagents; Stephan Daetwyler and Robert Ernst for help with image analysis and
566 script writing; the Live Cell Imaging Facility at UT Southwestern and Light Microscopy
567 Facility at the MPI-CBG for help with microscopy; the Protein Expression Facility at MPI-
568 CBG for help with protein expression.

569

570 AUTHOR CONTRIBUTIONS

571 M.M., A.W.F., and M.K. built the FLUCS microscope. M.M. and V.M.T. performed and
572 analyzed the FLUCS experiments on *C. elegans* embryos. M.U.R. performed the *spd-2*
573 temperature-sensitive experiments. B.F-G. and S.J.E. performed two-color imaging of
574 PCM proteins during anaphase and wrote the image analysis scripts. A.B. performed
575 imaging of *sur-6(RNAi)* mutants. J.B.W. purified proteins and performed the *in vitro*
576 assays. V.M.T. performed all other in vivo experiments and analysis. J.B.W. and M.K.
577 analyzed data and wrote the manuscript.

578

579 FIGURE LEGENDS

580 **Figure 1. FLUCS reveals changes in PCM deformation resistance and fracture**
581 **resistance during mitosis in *C. elegans* embryos.**

582 A. Diagram of mitotic progression in a one-cell *C. elegans* embryo (top panels). Force
583 generation (arrows) by cortically anchored microtubules aid in chromosome
584 segregation, spindle positioning, and PCM disassembly during telophase. Live-
585 cell confocal microscopy images of *C. elegans* embryos expressing a PCM marker
586 (mMaple::SPD-5) and DNA marker (mCherry::HistoneH2B).

587 B. Diagram of the FLUCS microscope setup (left) and generation of intracellular flows
588 after unidirectional scanning of a 1455 nm laser at 1500 Hz. Scan path is
589 represented by the magenta line. The magnitudes of local flow velocities are
590 reflected by arrow size.

591 C. Using FLUCS, flows (red arrows) are generated in the cytoplasm and pass through
592 the PCM (green ball). Microtubule-derived pulling forces (grey arrows) also exert
593 tensile stresses on PCM.

594 D. Tuning the power of the 1455 nm laser (25, 32, and 40 mW) generates three tiers
595 of flow velocity (LOW, MEDIUM, and HIGH). Individual data points are plotted with
596 mean +/- 95% CI; n = 5 measurements per condition.

597 E. Time lapse images of PCM morphology in anaphase after application of no flow
598 (OFF) or low, medium, and high flow. Orange heading boxes indicate when flow
599 occurs. Arrows indicate flow path and direction. Blue heading boxes indicate when
600 flow is turned off.

601 F. PCM was subjected to high-flow FLUCS during metaphase, anaphase, and
602 telophase.

603 G. For each FLUCS experiment, we measured the change in PCM length over time
604 (Deformation rate) and the frequency of complete separations in PCM (Fracture
605 probability).

606 H. PCM deformation rates were measured in metaphase, anaphase, and telophase
607 using low, medium, and high flow. Individual data points are plotted with mean +/-
608 95% CI; n = 7,6,7 (metaphase; LOW, MED, HIGH flow), n = 7,8,7 (anaphase), n =
609 7,8,9 (telophase) measurements per condition. 10 kHz bidirectional scanning of
610 the 1455 nm laser using 40 mW power, generates heat without producing flows
611 (TEMP control; n = 4,5,5 (metaphase, anaphase, telophase)). For high flow,
612 differences are statistically significant using a one-way ANOVA followed by a

613 Tukey's multiple comparison test (metaphase vs. anaphase, $p = 0.04$; metaphase
614 vs. telophase, $p = 0.0001$).

615 I. PCM fracture probabilities from experiments in (H). Sample numbers are the same
616 as in (H).

617

618 **Figure 2. PCM undergoes structural weakening during anaphase, independent of**
619 **cortical pulling forces.**

620 A. Time-lapse images of *gpr-1/2(RNAi)* embryos treated with 40 mW FLUCS (high
621 flow).

622 B. PCM deformation rates in metaphase (M), anaphase (A), and telophase (T) using
623 high flow in wild-type and *gpr-1/2(RNAi)* embryos. Wild-type data are from
624 experiments in Figure 1. Individual data points are plotted with mean +/- 95% CI;
625 $n = 7,7,9$ (wild-type; metaphase, anaphase, telophase) and $n = 10,12,14$ (*gpr-
626 1/2(RNAi)*).

627 C. PCM fracture probabilities from experiments in (B).

628 D. Permeabilized embryos were treated in metaphase or telophase with 10 μ g/ml
629 nocodazole, then subjected to high-flow FLUCS. Representative images are
630 shown on the left, line scans (dotted line in the inset) of fluorescence intensity
631 before and after FLUCS are on the right.

632 E. Zoomed in time-lapse images of PCM deformation under high-flow FLUCS in a
633 *gpr-1/2(RNAi)* embryo.

634 F. Plots comparing PCM length on the long axis orthogonal to flow direction over time.
635 Both high flow and medium flow induce PCM deformation.

636

637 **Figure 3. Discrete changes in PCM composition correlate with the PCM**
638 **weakening transition in anaphase.**

639 A. Diagram of *C. elegans* centrosome architecture and composition.

640 B. Worm lines were generated that express mCherry-labeled γ -tubulin (as a standard)
641 and 9 different GFP-labeled PCM proteins (left panels). Fluorescence intensity at
642 the PCM was measured over time (right panels).

643 C. Example images from dual-color, time-lapse recording of PCM disassembly in 9
644 different embryo lines described in (B).

645 D. Quantification of the experiments in B-C. For each strain, the plots represent the
646 normalized integrated fluorescence density of PCM-localized mCherry-tagged γ -
647 tubulin compared to the GFP-tagged protein from anaphase onward. Anaphase
648 was indicated by spindle rocking. Shown are the analyses for anterior-localized
649 centrosomes. Data were normalized to the maxima for each individual curve, then
650 these curves were averaged (mean +/- 95% C.I. n = 13 (γ -tubulin), 9 (PLK-1), 10
651 (SPD-2), 12 (SPD-5), 14, (RSA-1), 12 (RSA-2), 7 (TAC-1), 10 (TPXL-1), 13 (AIR-
652 1)).

653 E. The order of PCM protein departure was determined by calculating the time lag
654 between halfway points of PCM protein departure per strain (Δt_{EXIT}). Halfway
655 points were determined by fitting each curve during the window of linear departure.

656 F. Departure time lag (Δt_{EXIT}) of GFP-labeled PCM proteins relative to mCherry:: γ -
657 tubulin. A negative value indicates that the GFP-labeled protein departed before γ -
658 tubulin. A positive value indicates that the GFP-labeled protein departed after γ -
659 tubulin. Results for anterior centrosomes are shown (mean +/- 95% C.I.; sample
660 number is the same as in (D)). Statistical analyses are shown in Table S3.

661 G. Departure time lag (Δt_{EXIT}) of posterior-localized PCM proteins relative to
662 mCherry:: γ -tubulin. Sample number is the same as in (D). Statistical analyses are
663 shown in Table S4.

664

665 **Figure 4. Acute inhibition of PLK-1 and SPD-2 induces premature weakening and**
666 **disassembly of the PCM scaffold.**

667 A. PCM was subjected to high-flow FLUCS during metaphase in wild-type embryos
668 or permeabilized embryos treated with 10 μ M BI-2536 (inhibitor of Polo Kinases).
669 Permeabilized embryos behaved as wild-type embryos during the first cell division
670 (see methods; Carvalho 2011).

671 B. PCM deformation rates in metaphase using low, medium, and high flow in wild-
672 type and BI-2536-treated embryos. Wild-type data are from experiments in Figure
673 1. Individual data points are plotted showing mean +/- 95% CI; n = 6-7 (wild-type)

674 and n = 5-7 (BI-2536-treated). P-values were calculated using a Mann-Whitney
675 test.

676 C. PCM fracture probabilities from experiments in (B).

677 D. Permeabilized embryos were arrested in metaphase using 10 μ M MG-132, then
678 treated with 0.1% ethanol (no drug) or 10 μ M BI-2536. Data are plotted as
679 normalized lines representing mean +/- 95% CI; n = 8 (no drug) and n = 10 (BI-
680 2536-treated).

681 E. Embryos expressing GFP::SPD-5 and a temperature-sensitive version of SPD-2
682 (*spd-2(or188ts)*) were allowed to assemble centrosomes at the permissive
683 temperature (16°C), upshifted to the non-permissive temperature (25°C) for 1 min
684 during prometaphase, then subjected to high-flow FLUCS during metaphase.

685 F. For each experiment in *spd-2(or188ts)* embryos, one centrosome was subjected
686 to FLUCS and the other left alone (control). Integrated fluorescent intensities of
687 the SPD-5 signal were tracked over time, then normalized to the starting value.
688 Each curve represents a single experiment.

689 G. PCM fracture probabilities using low, medium, and high flow. Wild-type data are
690 reproduced from Figure 1. n = 7,7,8 (wild-type) and 5,6,8 (*spd-2(or188ts)*).

691 H. Embryos were upshifted from 16°C to 23°C during metaphase, then imaged during
692 anaphase. Data show integrated fluorescence densities of PCM-localized signal,
693 plotted as normalized lines representing mean +/- 95% CI; n = 24 centrosomes in
694 both wild-type and *spd-2(or188ts)* embryos.

695

696 **Figure 5. Polo Kinase and SPD-2 protect *in vitro* reconstituted PCM from induced
697 disassembly.**

698 A. *In vitro* SPD-5 condensate disassembly experiment. 500 nM SPD-5::TagRFP was
699 incubated in 9% PEG to induce spontaneous formation of micron-scale SPD-5
700 condensates (1. before). After 5 min, the condensates were pipetted harshly and
701 diluted 1:10 in PEG-free buffer, incubated for 10 min, then imaged (2. after).

702 B. Quantification of total SPD-5 condensate mass per field of view remaining after
703 dilution-induced disassembly. Buffer, 240 nM SPD-2, 500 nM constitutively active
704 PLK-1 (PLK-1^{CA}), and/or 500 nM kinase dead PLK-1 (PLK-1^{KD}) were added at the

705 beginning. The plot shows total integrated fluorescence density for each field of
706 view (red bars indicate mean +/- 95% C.I.; n >22 images per experiment).

707 C. Representative images from (B) before and after dilution-induced disassembly.
708

709 **Figure 6. PCM becomes fracture-resistant and ductile in anaphase after inhibition**
710 **of PP2A phosphatase.**

711 A. PCM was subjected to high-flow FLUCS during anaphase in wild-type embryos
712 or permeabilized embryos treated with 10 μ M LB-100 (inhibitor of PP2A
713 phosphatase).

714 B. PCM deformation rates in anaphase using high flow in wild-type and LB-100-
715 treated embryos. Wild-type data are from experiments in Figure 1. Individual data
716 points are plotted with bars representing mean +/- 95% CI; n = 7 (wild-type) and
717 10 (LB-100-treated) centrosomes. P-values were calculated using a Mann-
718 Whitney test.

719 C. Ratio of final PCM length to original length in experiments from (B). Original PCM
720 length was measured before flow began and final PCM length was measured once
721 flow was turned off. P-values were calculated using a Mann-Whitney test.

722 D. PCM fracture probabilities for high-flow FLUCS in metaphase (M), anaphase (A),
723 and telophase (T). Wild-type data are from experiments in Figure 1; n= 8,11,11
724 (wild-type) and 7,9,6 (LB-100-treated) centrosomes.

725 E. Permeabilized embryos were treated with no drug or 10 μ M LB-100 in metaphase,
726 then imaged until 300s after anaphase onset. Data are plotted as normalized lines
727 representing mean +/- 95% CI; n = 24 (no drug) and n = 21 (LB-100-treated)
728 centrosomes.

729 F. Dual-color imaging of embryos expressing GFP-tagged LET-92, the PP2A
730 catalytic subunit in *C. elegans* (GFP::PP2Ac), and SPD-5::mCherry. Data are
731 plotted as normalized lines representing mean +/- 95% CI; n = 10 centrosomes.
732

733 **Figure 7. The balance of PLK-1, SPD-2, and PP2A activities tune PCM strength and**
734 **ductility.**

735 A. PCM resistance to microtubule-mediated forces peaks in metaphase during
736 spindle assembly, then declines in anaphase and telophase, corresponding to
737 PCM disassembly.

738 B. PCM-localized levels of 8 different proteins during mitotic progression. In
739 anaphase, PLK-1 levels decline first, followed by SPD-2. The catalytic subunit of
740 PP2A phosphatase (PP2Ac), as well as the main scaffold protein SPD-5, remain
741 at the PCM until late telophase.

742 C. In metaphase, FLUCS cannot fracture or deform wild-type PCM. However, FLUCS
743 can fracture PCM in *spd-2* mutant embryos (i.e., PCM is less ductile) and stretch
744 and deform PCM in PLK-1 inhibited embryos (i.e., PCM is less strong but still
745 ductile). In anaphase, FLUCS easily deforms and fractures wild-type PCM, while
746 it deforms and stretches PCM in PP2A-inhibited embryos (i.e., PCM is more
747 ductile).

748 D. The combination of PP2A phosphatase activity and the departure of PLK-1 and
749 SPD-2 transitions PCM from a strong, ductile state in metaphase to a weak, brittle
750 state in telophase. This transition enables PCM disassembly and dispersal through
751 microtubule-mediated pulling forces.

752

753 **SUPPLEMENTAL FIGURE LEGENDS**

754 **Figure S1. FLUCS control experiments.**

755 A. Power law scaling of cytoplasmic flow with increasing FLUCS laser power.
756 Individual data points represent mean +/- 95% CI; n = 5 embryos per laser
757 condition. Flow velocities were fit with a second-order polynomial.

758 B. Application of high-flow FLUCS in an anaphase 1-cell embryo. Images are pseudo-
759 colored to highlight the subtle increase in cytoplasmic mMaple::SPD-5
760 fluorescence after flow begins. Note: the centrosome goes out of focus in the first
761 frame when FLUCS begins.

762 C. Application of high-flow FLUCS in a prometaphase 1-cell embryo. Single plane
763 images are shown. Flow causes the centrosome to leave the plane of focus at t=0s
764 and t=20s. Flow then displaces the centrosome toward the cortex.

765 D. High-flow FLUCS was applied in metaphase, continuing into anaphase (indicated
766 by chromosome segregation at t=12s).

767 E. Example images from the experiment in Figure 1H. Bidirectional scanning of a 40
768 mW laser (1455 nm) at 10 kHz creates local temperature gradients without
769 generating flow.

770 F. Time-lapse fluorescence and brightfield images of an embryo after cessation of
771 FLUCS. Application of high-flow FLUCS does not affect embryonic development.

772

773 **Figure S2. Contributions of microtubule pulling forces to PCM deformation.**

774 A. PCM deformation rates in metaphase (M), anaphase (A), and telophase (T)
775 using high flow in wild-type and *gpr-1/2(RNAi)* embryos or 40 mW bidirectional
776 laser scanning (temperature control; no flow). Data are from experiments in
777 Figures 1 and 2. Individual data points are plotted with mean +/- 95% CI; n =
778 7,7,9 (wild-type; metaphase, anaphase, telophase), n = 10,12,13 (*gpr-1/2(RNAi)*) and n = 4,5,5 (temperature control). P values were calculated using
779 Brown-Forsythe and Welch ANOVA tests followed by Dunnett's T3 multiple
780 comparisons tests.

781 B. Time-lapse images of centrosomes in a *csnk-1(RNAi)* embryo, where
782 microtubule-mediated pulling forces at the cortex are ~1.5-fold elevated
783 compared to wild type (Panbianco et al., 2008). PCM deformation does not
784 occur prematurely in metaphase.

785

786

787 **Figure S3. Localization profiles of PCM proteins in the posterior embryo during**
788 **PCM disassembly.**

789 Quantification of PCM localization in the posterior side of 1-cell embryos in Figure
790 3. For each strain, the plots represent the normalized integrated fluorescence
791 density of PCM-localized mCherry-tagged γ -tubulin compared to the GFP-tagged
792 protein from anaphase onward. Anaphase was indicated by spindle rocking. Data
793 are normalized to maxima for each individual curve, then averaged; mean +/- 95%
794 C.I. n = 13 (γ -tubulin), 9 (PLK-1), 10 (SPD-2), 12 (SPD-5), 14, (RSA-1), 12 (RSA-
795 2), 7 (TAC-1), 10 (TPXL-1), 13 (AIR-1)).

796

797 **Figure S4. FLUCS and localization experiments in *sur-6(RNAi)* embryos.**

798 A. High-flow FLUCS was applied to a centrosome in an embryo depleted of SUR-6,
799 a PP2A regulatory subunit involved in PCM disassembly.

800 B. PCM deformation rates in anaphase during high-flow FLUCS in wild-type and *sur-*
801 *6(RNAi)* embryos. Wild-type data are from experiments in Figure 1. Individual data
802 points are plotted with bars representing mean +/- 95% CI; n = 7 (wild-type) and
803 10 (*sur-6(RNAi)*) centrosomes.

804 C. PCM fracture probabilities in metaphase (M), anaphase (A), and telophase (T)
805 during high-flow FLUCS experiments. N= 8-11 (wild-type) and 8-17 (*sur-6(RNAi)*)
806 centrosomes.

807 D. Images of PCM-localized GFP::PLK-1 in wild-type and *sur-6(RNAi)* embryos.

808 E. Normalized integrated fluorescence intensity of PCM-localized GFP::SPD-2
809 during anaphase. Data are plotted as mean +/- 95% CI; n= 22 (wild-type) and 32
810 (*sur-6(RNAi)*) centrosomes.

811 F. Images of PCM-localized GFP::SPD-2 in wild-type and *sur-6(RNAi)* embryos.

812 G. Normalized integrated fluorescence intensity of PCM-localized GFP::SPD-2
813 during anaphase. Data are plotted as mean +/- 95% CI; n= 20 (wild-type) and 24
814 (*sur-6(RNAi)*) centrosomes.

815

816 **SUPPLEMENTAL MOVIES**

817 **Movie S1. FLUCS flow control using 25 mW, 32 mW, and 40 mW laser scans at 1.5**

818 **kHz.** Flows were generated in *C. elegans* 1-cell embryos using three different 1455 nm
819 laser powers (25 mW, 32 mW, and 40 mW).

820 **Movie S2. High-flow FLUCS targeting the centrosome in a prometaphase 1-cell**

821 **embryo.** Prometaphase *C. elegans* embryos expressing mCherry::histoneH2B

822 (magenta) and GFP::SPD-5 (green) were subjected to high-flow FLUCS (40 mW).

823 Images are of a single confocal plane.

824 **Movie S3. High-flow FLUCS targeting the centrosome in a metaphase 1-cell**

825 **embryo.** Metaphase *C. elegans* embryos expressing mCherry::histoneH2B (magenta)

826 and GFP::SPD-5 (green) were subjected to high-flow FLUCS (40 mW). Images are of a
827 single confocal plane.

828 **Movie S4. High-flow FLUCS targeting the centrosome in an anaphase 1-cell**
829 **embryo.** Anaphase *C. elegans* embryos expressing mCherry::histoneH2B (magenta)
830 and GFP::SPD-5 (green) were subjected to high-flow FLUCS (40 mW). Images are of a
831 single confocal plane.

832 **Movie S5. High-flow FLUCS targeting the centrosome in a telophase 1-cell**
833 **embryo.** Telophase *C. elegans* embryos expressing mCherry::histoneH2B (magenta)
834 and GFP::SPD-5 (green) were subjected to high-flow FLUCS (40 mW). Images are of a
835 single confocal plane.

836 **Movie S6. High-flow FLUCS targeting the centrosome during the metaphase to**
837 **anaphase transition in a 1-cell embryo.** *C. elegans* embryos expressing
838 mCherry::histoneH2B (magenta) and GFP::SPD-5 (green) were subjected to high-flow
839 FLUCS (40 mW) during the metaphase-anaphase transition. Images are of a single
840 confocal plane.

841

842 **TABLE S1. *C. elegans* strains used in this study**

Strain name	genotype	Creation method	Origin
DAM858	vie11[pAD676; gfp::tac-1]II	CRISPR	Alexander Dammermann
EU584	spd-2(or188ts) I	mutagenesis	Bruce Bowerman
JWW1	utsw2[mMaple::spd-5] I	CRISPR	This study
JWW13	spd-2(or188ts) I; unc-119(ed9) III; ltsi202[pVV103/ pOD1021; Pspd-2::GFP::SPD-5 RNAiresistant; cb-unc-119(+)]II	Cross of EU584 and OD847	This study
JWW35	ltsi202[pVV103/ pOD1021; Pspd-2::GFP::SPD-5 RNAiresistant; cb-unc-119(+)]II ; unc-119(ed3)III; ddls44[WRM0614cB02 GLCherry::tbg-1; Cbr-unc-119(+)]	Cross of OD847 and TH169	This study
JWW64	utsw2[mMaple::spd-5] I; lts37 [(pAA64) pie-1p::mCherry::his-58 + unc-119(+)] IV.	Cross of JWW1 and OD95	This study
JWW65	lts17[plk-1::gfp+loxP]III ; lts37 [(pAA64) pie-1p::mCherry::his-58 + unc-119(+)] IV; unc-119(ed3) III	Cross of OD2425 and OD95	This study
JWW66	ltsi203[pVV60; Pspd-2::GFP::SPD-2 reencoded; cb-unc-119(+)]II; lts37 [(pAA64) pie-1p::mCherry::his-58 + unc-119(+)] IV; unc-119(ed3) III	Cross of OD824 and OD95	This study

JWW67	unc-119(ed9) III; utsW1[pJWB56; Pspd-2::GFP::SPD-5(530E, 627E, 653E, 658E) re-encoded; cb-unc-119(+)] III	MosSCI, into EG6699	This study
JWW69	unc-119(ed9) III; ltsi202[pVV103/ pOD1021; Pspd-2::GFP::SPD-5 RNAiresistant; cb-unc-119(+)] III; lts37 [(pAA64) pie-1p::mCherry::his-58 + unc-119(+)] IV.	Cross of OD847 and OD95	This study
JWW70	unc-119(ed9) III; utsW1[pJWB56; Pspd-2::GFP::SPD-5(530E, 627E, 653E, 658E) re-encoded; cb-unc-119(+)] III; lts37 [(pAA64) pie-1p::mCherry::his-58 + unc-119(+)] IV.	Cross of JWW1 and OD95	This study
JWW71	lt17[plk-1::gfp+loxP] III; unc-119(ed3) III; ddls44[WRM0614cB02 GLCherry::tbg-1; Cbr-unc-119(+)]	Cross of OD2425 and TH169	This study
JWW72	vie11[pAD676; gfp::tac-1] II; unc-119(ed3) III; ddls44[WRM0614cB02 GLCherry::tbg-1; Cbr-unc-119(+)]	Cross of DAM858 and TH169	This study
JWW89	spd-2(or188ts) I; ltsi202[pVV103/ pOD1021; Pspd-2::GFP::SPD-5 RNAiresistant; cb-unc-119(+)] III; lts37 [(pAA64) pie-1p::mCherry::his-58 + unc-119(+)] IV.	Cross of JWW13 and OD95	This study
OD2425	lt17[plk-1::gfp+loxP] III	CRISPR	Karen Oegema
OD823	ltsi203[pVV60; Pspd-2::GFP::SPD-2 reencoded; cb-unc-119(+)] II; unc-119(ed3) III	MosSCI, into EG6699	Karen Oegema
OD847	unc-119(ed9) III; ltsi202[pVV103/ pOD1021; Pspd-2::GFP::SPD-5 RNAiresistant; cb-unc-119(+)] III	MosSCI, into EG6699	(Woodruff et al., 2015)
OD95	unc-119(ed3) III; lts37 [(pAA64) pie-1p::mCherry::his-58 + unc-119(+)] IV; lts38 [pie-1p::GFP::PH(PLC1delta1) + unc-119(+)]	Microparticle bombardment	CGC
TH169	unc-119(ed3) III; ddls44[WRM0614cB02 GLCherry::tbg-1; Cbr-unc-119(+)]	Microparticle bombardment	Anthony Hyman
TH447	unc-119(ed9) III; ddls243[pie-1p::LAP::LET-92; unc-119(+)]; ddls247[pie-1p::SPD-5(synthetic introns, CAI 0.65)::mCherry; unc-119(+)]	Microparticle bombardment	Anthony Hyman
TH530	rsa-1::LAP; unc-119(ed3) III; ddls44[WRM0614cB02 GLCherry::tbg-1; Cbr-unc-119(+)]	Microparticle bombardment	Anthony Hyman
TH531	rsa-2::LAP; unc-119(ed3) III; ddls44[WRM0614cB02 GLCherry::tbg-1; Cbr-unc-119(+)]	Microparticle bombardment	Anthony Hyman
TH539	spd-2::GFP; unc-119(ed3) III; ddls44[WRM0614cB02 GLCherry::tbg-1; Cbr-unc-119(+)]	Microparticle bombardment	Anthony Hyman
TH571	unc-119(ed3) III; ddls12[pie-1p::tpxl-1::GFP; unc-119(+)]; ddls44[WRM0614cB02 GLCherry::tbg-1; Cbr-unc-119(+)]	Microparticle bombardment	Anthony Hyman
TH630	ddls44[WRM0614cB02 GLCherry::tbg-1; Cbr-unc-119(+)]; ddls62[pie-1p::AIR-1(synthetic introns, CAI 1.0)::GFP; unc-119(+)]; unc-119(ed3) III	Microparticle bombardment	Anthony Hyman
EG6699	ttTi5605 II; unc-119(ed3) III; oxEx1578.		CGC

843

844

845 **TABLE S2. Protein expression plasmids used in this study**

Plasmid name	Gene	N-term tag	C-term tag	Origin
JWV11	<i>plk-1(T194D)</i> constitutively active		PreScission-6xHis	(Woodruff et al., 2015)
JWV12	<i>plk-1(K67M)</i> kinase dead		PreScission-6xHis	(Woodruff et al., 2015)
JWV2	<i>spd-5(wt)</i>	MBP- PreScission	PreScission-6xHis	(Woodruff et al., 2015)
JWV3	<i>spd-5(wt)</i>	MBP- PreScission	tagRFP- PreScission-6xHis	(Woodruff et al., 2015)
JWV6	<i>spd-2(wt)</i>	MBP-TEV	TEV-6xHis	(Woodruff et al., 2015)

846

847 **TABLE S3. One-way ANOVA and post-hoc tests of anterior PCM disassembly**
 848 **profiles from Figure 3F**

Holm-Sidak's multiple comparisons test	Mean Diff.	Significant?	Summary	Adjusted P Value
AIR-1 vs. TPXL-1	-25.55	No	ns	0.2725
AIR-1 vs. RSA-1	-8.310	No	ns	0.9615
AIR-1 vs. RSA-2	-14.38	No	ns	0.8174
AIR-1 vs. SPD-2	38.26	Yes	**	0.0079
AIR-1 vs. SPD-5	-24.73	No	ns	0.2183
AIR-1 vs. TBG-1	8.728	No	ns	0.9598
AIR-1 vs. TAC-1	0.4412	No	ns	0.9963
AIR-1 vs. PLK-1	92.29	Yes	****	<0.0001
TPXL-1 vs. RSA-1	17.24	No	ns	0.8060
TPXL-1 vs. RSA-2	11.16	No	ns	0.9598
TPXL-1 vs. SPD-2	63.81	Yes	****	<0.0001
TPXL-1 vs. SPD-5	0.8171	No	ns	0.9963
TPXL-1 vs. TBG-1	34.28	Yes	*	0.0356
TPXL-1 vs. TAC-1	25.99	No	ns	0.4307
TPXL-1 vs. PLK-1	117.8	Yes	****	<0.0001
RSA-1 vs. RSA-2	-6.074	No	ns	0.9615
RSA-1 vs. SPD-2	46.57	Yes	**	0.0012
RSA-1 vs. SPD-5	-16.42	No	ns	0.8060
RSA-1 vs. TBG-1	17.04	No	ns	0.7693
RSA-1 vs. TAC-1	8.751	No	ns	0.9615
RSA-1 vs. PLK-1	100.6	Yes	****	<0.0001
RSA-2 vs. SPD-2	52.64	Yes	****	<0.0001
RSA-2 vs. SPD-5	-10.35	No	ns	0.9598
RSA-2 vs. TBG-1	23.11	No	ns	0.2887
RSA-2 vs. TAC-1	14.83	No	ns	0.8971
RSA-2 vs. PLK-1	106.7	Yes	****	<0.0001
SPD-2 vs. SPD-5	-62.99	Yes	****	<0.0001
SPD-2 vs. TBG-1	-29.53	No	ns	0.0940

SPD-2 vs. TAC-1	-37.82	Yes	*	0.0454
SPD-2 vs. PLK-1	54.03	Yes	***	0.0002
SPD-5 vs. TBG-1	33.46	Yes	*	0.0207
SPD-5 vs. TAC-1	25.17	No	ns	0.4085
SPD-5 vs. PLK-1	117.0	Yes	****	<0.0001
TBG-1 vs. TAC-1	-8.286	No	ns	0.9615
TBG-1 vs. PLK-1	83.56	Yes	****	<0.0001
TAC-1 vs. PLK-1	91.85	Yes	****	<0.0001

849

850 **TABLE S4. One-way ANOVA and post-hoc tests of posterior PCM disassembly**
 851 **profiles from Figure 3G**

Holm-Sidak's multiple comparisons test	Mean Diff.	Significant?	Summary	Adjusted P Value
AIR-1 vs. TPXL-1	-9.235	No	ns	0.9002
AIR-1 vs. RSA-1	-36.70	Yes	***	0.0003
AIR-1 vs. RSA-2	-46.04	Yes	****	<0.0001
AIR-1 vs. SPD-2	5.014	No	ns	0.9652
AIR-1 vs. SPD-5	-42.30	Yes	****	<0.0001
AIR-1 vs. TBG-1	-13.68	No	ns	0.5679
AIR-1 vs. TAC-1	-34.04	Yes	**	0.0041
AIR-1 vs. PLK-1	40.38	Yes	****	<0.0001
TPXL-1 vs. RSA-1	-27.46	Yes	*	0.0334
TPXL-1 vs. RSA-2	-36.81	Yes	***	0.0006
TPXL-1 vs. SPD-2	14.25	No	ns	0.6655
TPXL-1 vs. SPD-5	-33.07	Yes	**	0.0028
TPXL-1 vs. TBG-1	-4.446	No	ns	0.9652
TPXL-1 vs. TAC-1	-24.80	No	ns	0.1399
TPXL-1 vs. PLK-1	49.61	Yes	****	<0.0001
RSA-1 vs. RSA-2	-9.346	No	ns	0.9002
RSA-1 vs. SPD-2	41.71	Yes	****	<0.0001
RSA-1 vs. SPD-5	-5.608	No	ns	0.9652
RSA-1 vs. TBG-1	23.02	No	ns	0.0790
RSA-1 vs. TAC-1	2.661	No	ns	0.9652
RSA-1 vs. PLK-1	77.07	Yes	****	<0.0001
RSA-2 vs. SPD-2	51.06	Yes	****	<0.0001
RSA-2 vs. SPD-5	3.739	No	ns	0.9652
RSA-2 vs. TBG-1	32.36	Yes	**	0.0014
RSA-2 vs. TAC-1	12.01	No	ns	0.8399
RSA-2 vs. PLK-1	86.42	Yes	****	<0.0001
SPD-2 vs. SPD-5	-47.32	Yes	****	<0.0001
SPD-2 vs. TBG-1	-18.70	No	ns	0.2609
SPD-2 vs. TAC-1	-39.05	Yes	**	0.0014
SPD-2 vs. PLK-1	35.36	Yes	**	0.0020
SPD-5 vs. TBG-1	28.62	Yes	**	0.0061
SPD-5 vs. TAC-1	8.269	No	ns	0.9307
SPD-5 vs. PLK-1	82.68	Yes	****	<0.0001

TBG-1 vs. TAC-1	-20.35	No	ns	0.2689
TBG-1 vs. PLK-1	54.06	Yes	****	<0.0001
TAC-1 vs. PLK-1	74.41	Yes	****	<0.0001

852

853

854 **METHODS**

855 **Contact for reagent and resource sharing**

856 Further requests and information for resources and reagents should be directed to and
857 will be fulfilled by the Lead Contact, Jeffrey Woodruff

858 (Jeffrey.woodruff@utsouthwestern.edu).

859

860 **Experimental model and subject details**

861 *C. elegans* worm strains were grown on nematode growth media (NGM) plates at 16-
862 23°C, following standard protocols (www.wormbook.org). Worm strains used in this study
863 are listed in Table S1 and created using CRISPR (Paix et al., 2015; Paix et al., 2017),
864 MosSCI (Frokjaer-Jensen et al., 2008), or microparticle bombardment. Cas9 enzyme was
865 purified by the Protein Expression Facility at MPI-CBG. For expression of recombinant
866 proteins, we used suspended SF9-ESF *S. frugiperda* insect cells grown at 27°C in ESF
867 921 Insect Cell Culture Medium, Protein-Free (Expression Systems), supplemented with
868 Fetal Bovine Serum (2% final concentration).

869

870 **RNAi treatment**

871 RNAi was done by feeding using *sur-6*, *gpr-2*, *csnk-1*, and *perm-1* feeding clones from
872 the Ahringer and Vidal collections (Source BioScience)(Rual et al., 2004). The *spd-5*
873 feeding clone targets a region that is reencoded in our MosSCI transgenes (Woodruff et
874 al., 2015). Bacteria were seeded onto nematode growth media (NGM) supplemented
875 with 1 mM isopropyl β-D-1-thiogalactopyranoside (IPTG) and 100 µg mL⁻¹ ampicillin.
876 For *perm-1* feeding plates, 0.1 mM IPTG was used. L4 hermaphrodites were grown at
877 23°C for 24-28 hours for all conditions except for *perm-1*, which was at 20°C for 18-19
878 hours.

879

880 **Drug treatment of semi-permeable embryos**

881 For all drug treatments, *C. elegans* embryos were permeabilized using *perm-1* RNAi
882 (Carvalho et al., 2011) and dissected into a 62% solution of ESF-921 Media (Expression
883 Systems). To arrest the embryos at metaphase, MG-132 (EMD Millipore) was used at 10
884 μ M in 62% ESF, diluted from a 10 mM stock concentration in EtOH. To inhibit PLK-1,
885 BI-2536 (Advanced ChemBlocks Inc.) was used at 10 μ M, diluted from a 10 mM stock
886 in ethanol. To inhibit PP2A, LB-100 (SelleckChem) was used at 10 μ M, diluted from a
887 10 mM stock in dH₂O. Nocodazole (Sigma) was diluted from a 5 mg/ml stock
888 concentration in DMSO. Samples were flushed with water or M9 after each experiment
889 to test for permeability (water will cause swelling and M9 will cause shrinking).

890

891 **Construction of the FLUCS Microscope**

892 To measure the physical material state of centrosomes inside living *C. elegans* embryos,
893 we performed intracellular flow perturbations by employing the previously published
894 technology FLUCS (Mittasch et al., 2018). The FLUCS setup consisted of three major
895 modules: (i) an infrared laser scanning unit for thermal manipulations, (ii) a microscope
896 allowing to simultaneously induce thermal patterns and to perform high-sensitivity
897 fluorescence imaging, and (iii) a heat management stage.

898 (i) The infrared laser scanning unit consists of a fiber-based infrared Raman laser (CRFL-
899 20-1455-OM1, 20 Watts, near TEM00 mode profile, Keopsys, France) with a wavelength
900 of 1455 nm, operated in continuous-wave mode and linearly polarized using a polarizing
901 beam splitter cube (CCM1-PBS254, Thorlabs, USA). To precisely correct for the
902 divergence of the laser beam, a telescope was used, composed of two telescope lenses
903 with focal lengths of f_1=100 mm and f_2=150 mm (AC254-C series, Thorlabs, USA),
904 respectively. A lambda-half plate (waveplate, 1/2 1550 Edmund optics, USA) was used
905 to rotate the linearly polarized laser light to match the optical axis of the acoustic-optical
906 deflector (AOD). A variable optical beam expander (4x expander, 36100, Edmund optics,
907 USA) allows control of the beam diameter (~1.5 mm beam diameter at back-focal-plane
908 was used) without changing the size of the scan pattern. Rapid (up to 1 MHz update rate)
909 and precise (down to 100 nm) infrared laser scanning was achieved by utilizing two-
910 dimensional AOD (AA.DTSXY-A6-145, Pegasus Optik, Germany), electronic oscillators
911 (AA.DRFAI0Y-B-0-x, Pegasus Optik, Germany), and electronic amplifiers 2.5 W

912 (AA.AMPA-B-34-20.4, Pegasus Optik, Germany). The AOD was controlled by generating
913 analog signals using a custom software in LabVIEW (National instruments, USA) in
914 combination with a PCI controller card (PCIe 6369, National Instruments, USA). To
915 precisely translate the AOD-induced beam scanning into the back-focal-plane of the
916 microscope objective lens a telescope composed of two telescope lenses with focal
917 lengths of $f_3=f_4=300$ mm (AC254-C series, Thorlabs, USA) was used. A dichroic mirror
918 (F73-705, AHF, Germany) was used to couple the infrared laser beam into the light path
919 of the microscope (IX83, Olympus, Japan), by selectively reflecting the infrared light but
920 transmitting visible wavelengths which were used for fluorescence imaging.

921

922 (ii) The microscope was equipped with Brightfield (BF) and fluorescent imaging optics.
923 For simultaneous high-resolution fluorescence imaging and precise infrared laser
924 scanning, an infrared-coated microscope objective lens (60x UPLSAPO NA=1.2, W-IR
925 coating, Olympus, Japan) was used, which was operated with heavy water (D₂O) as
926 immersion liquid to reduce undesired infrared laser light absorption in the immersion
927 layer. For Brightfield illumination a high-power LED (M565L3, Thorlabs, USA) in
928 combination with dedicated LED driver (LEDD1B, Thorlabs, USA) was used. For confocal
929 fluorescence imaging, a VisiScope confocal imaging system (Visitron, Germany) coupled
930 to a Yokogawa CSU-X1- A12 scan head and an iXON Ultra EMCCD camera (Andor,
931 Ireland) were used.

932

933 (iii) The heat management unit consisted of a thin sample mounting chamber based on a
934 standard cover slip (18 × 18 × 0.17 mm) (Menzel, Germany) facing the objective lens, and
935 a high thermal conductive sapphire cover slide (thermal conductivity of 27.1 W/m · K,
936 SMS-7521, UQG Optics, UK) closing the sandwich-like chamber from the top. To
937 efficiently remove the induced heat from the samples, e.g. *C. elegans* embryos, the
938 sapphire slide was actively cooled from room temperature to 17 °C. This active cooling
939 was performed by using Peltier elements (TES1-127021, TEC, Conrad) glued to the
940 sapphire slides. The cooling power of the Peltier elements was controlled by a PID
941 hardware controller (TEC-1089-SV, Meerstetter Engineering, Swiss). A custom-built
942 water-cooling stage was used to dissipate the heat produced by the Peltier elements. The

943 height of the buffer-filled chamber was defined using polystyrene beads (Polybead,
944 Polysciences, Germany) with a diameter of 15 μm . The height of the resulting chamber
945 was measured by locating the upper and lower chamber surface using a piezo stage.
946

947 **Application of FLUCS within embryos**

948 Late L4 hermaphrodites were grown for 18-19 hours on standard NGM or *perm-1* feeding
949 plates. Worms were then dissected on an 18 mm x 18 mm coverslip (0.17 mm thickness)
950 in 6 μL of M9 buffer or 62% ESF 921 (for permeabilized embryos) with 15 μm polystyrene
951 beads. The sample was placed onto a sapphire microscope slide equipped with Peltier
952 cooling elements, then the coverslip sealed with dental silicone (Picodent twinsil, Picodent,
953 Germany). The cooling stage and sample were then mounted on the FLUCS microscope
954 stage. Embryos were identified and staged using a 10x air objective, then imaged with a
955 60x 1.2 NA Plan Apochromat water immersion objective (Olympus) using 488 nm and
956 561 nm laser illumination, 1X1 binning, and 2s intervals.

957 Hydrodynamic flows were generated by scanning the 1455 nm laser through either 1)
958 center of centrosome or 2) through the cytoplasm for velocity calibration. Custom-written
959 LabVIEW software superimposes the scan path of the infrared laser with the high-
960 resolution image of the camera. The sub-pixel alignment of the induced flow field and the
961 camera image was verified routinely before the embryonic experiments by using
962 fluorescent tracer particles immersed in a highly viscous sucrose solution. FLUCS
963 experiments used unidirectional but repeated laser scans with 1.5 kHz scan frequency, a
964 scan length of 30 μm , and three different laser powers (25 mW, 32 mW, and 40 mW).

965 Centrosomes were targeted for FLUCS at metaphase, anaphase, or telophase.
966 Centrosomes were affected by FLUCS between 30-60 s. For experiments requiring drug
967 treatment, worms were dissected in 6 μL of the specific drug solution and quickly placed
968 on the microscope within 1-2 minutes. To maintain consistency of drug treatment
969 duration, only embryos found exactly at prometaphase (for metaphase experiments) and
970 metaphase (for anaphase experiments) were then targeted for FLUCS. Temperature-
971 sensitive worms were dissected in cold 62% ESF-921 media on a cooled dissecting scope
972 and quickly mounted onto the cooling stage, which was maintained at 17°C. At

973 prometaphase, temperature was upshifted to 25°C for 1 minute, then decreased to 17°C.
974 Centrosomes were then targeted for FLUCS at metaphase.

975
976 **Confocal microscopy and live-cell imaging**
977 Adult worms were dissected in M9 before being mounted on a 5% agar pad for imaging.
978 For live cell imaging with drug treatments, *perm-1* adult worms were dissected in 8-10 µL
979 of 62% ESF 921 with 15 µm polystyrene beads (Sigma-Aldrich) on a 22 x 50 mm
980 coverslip. Samples were mounted on a 1 mm thick glass slide with 2 x 6 mm laser cut
981 holes 30 mm apart (Potomac), to produce a flow chamber. In one open chamber, 40 µL
982 of the drug solution in 62% ESF was added during prometaphase. Liquid was wicked
983 from the opposite chamber using a Kimwipe to then allow more of the drug solution to be
984 added to the sample. To arrest embryos in metaphase, *perm-1* adult worms were
985 dissected in 10 µM MG-132 solution. Cell cycle stage was indicated based on
986 mCherry::HIS-58 fluorescence and cell morphology (metaphase = aligned chromosomes;
987 anaphase = chromosomes separate; telophase = chromosomes de-condense and
988 cytokinetic furrow ingresses).

989
990 Time-lapse images were taken using an inverted Nikon Eclipse Ti microscope with a
991 Yokogawa spinning disk confocal head (CSU-X1), piezo Z stage, and an iXon Ultra
992 EMCCD camera (Andor), controlled by Metamorph software. On this system, the 60x 1.4
993 NA Apochromat oil objective was used to acquire 36 x 0.5 µm Z-stacks every 10 seconds
994 with 100 ms exposures and 2X2 binning. For PCM localization in *csnk-1(RNAi)* embryos,
995 and PP2A localization, time-lapse images were acquired with an inverted Nikon Eclipse
996 Ti2-E microscope with a Yokogawa confocal scanner unit (CSU-W1), piezo Z stage, and
997 an iXon Ultra 888 EMCCD camera (Andor), controlled by Nikon Elements software. For
998 most experiments, we used a 60x 1.2 NA Plan Apochromat water immersion objective to
999 acquire 35 x 0.5 µm Z-stacks every 10 seconds with 100 ms exposures and 2X2 binning.
1000 Simultaneous imaging with the 488 nm and 561 nm lasers was achieved using an
1001 OptoSplit II beam splitter (Cairn). For LET-92::GFP imaging, a 100x 1.35 NA Plan
1002 Apochromat silicone oil objective was used to acquire 11 x 0.5 µm Z-stacks in 20 second
1003 intervals with 100 ms exposures and 2X2 binning. Images in Figure 3 were taken using

1004 an inverted Olympus IX81 microscope with a Yokogawa spinning-disk confocal head
1005 (CSU-X1), a 60x 1.2 NA Plan Apochromat water objective, and an iXon EM + DU-897 BV
1006 back illuminated EMCCD (Andor).

1007

1008 ***spd-2(or188ts)* temperature shift assay**

1009 JWW69 (control) and JWW89 (*spd-2(or188ts)*) strains were used for imaging.
1010 Sequencing of JWW89 confirmed a single point mutation in *spd-2* resulting in a glycine
1011 to glutamic acid amino acid substitution (G615E) as described in Kemp et. al. Both worm
1012 strains propagated at 16°C, which is the permissive temperature for *spd-2(or188ts)*. To
1013 prepare the embryos for imaging, a metal block was buried halfway in wet ice. A 24x60
1014 mm glass coverslip (thickness of 1) and a flow chamber slide were placed over the cold
1015 block. To prevent sticking of the glass to the cold block due to water condensation, two
1016 Kimwipes were placed between the glass and the cold block. To minimize exposure to
1017 elevated temperatures during embryo dissection, the glass stage on the dissecting
1018 microscope stand was placed in a 4°C fridge and left to cool for approximately 10 min.
1019 Once everything was cold, 10µL of cold M9 plus 15 µm polystyrene (Sigma) beads was
1020 pipetted to the middle of the 24x60 mm cover slip.

1021

1022 For each worm strain, plates were transported inside the ice bucket directly contacting
1023 ice to the dissecting microscope area. The microscope glass stage was taken out from
1024 the fridge and assembled into its place. Three to four adult worms containing a single row
1025 of eggs were transferred to the M9 plus beads on the cover slip still located on top of the
1026 cold block. The coverslip was transferred to the dissecting scope and the worms cut open
1027 using 22G needles. The coverslip was mounted on the flow chamber slide, then the edges
1028 of the cover slip were sealed using clear nail polish. The sample was moved to the
1029 imaging room on the cold block.

1030

1031 The Nikon Eclipse Ti2 microscope described above was used for imaging. Embryos were
1032 staged using a 10X air objective, then imaged with a 60X NA 1.2 water objective. To
1033 rapidly raise the temperature of the sample (up-shift), 40 µl of 25°C M9 was pipetted into
1034 the flow chamber well. 30 x 0.5 µm Z stacks were collected every 10 s using simultaneous

1035 illumination with 488 nm and 561 nm lasers (14.7% and 17.7% intensity respectively),
1036 2x2 binning, 100 ms exposures.

1037

1038 **Protein expression and purification**

1039 All expression plasmids are listed in Table S2. SPD-5, SPD-2, and PLK-1 proteins were
1040 expressed using the FlexiBAC baculovirus system (Lemaitre et al., 2019) and purified as
1041 previously described (Woodruff and Hyman, 2015; Woodruff et al., 2015), with the
1042 following exception: SPD-2 was stored in its uncleaved form (MBP-TEV-SPD-2).

1043

1044 ***In vitro* SPD-5 condensate disassembly assay**

1045 SPD-5 condensates were formed by diluting 10 μ M SPD-5 (1:10 mixture of SPD-5 and
1046 SPD-5::TagRFP) in Condensate buffer (25 mM HEPES, pH 7.4, 150 mM KCl) containing
1047 polyethylene glycol 3350 (Sigma) and fresh 0.5 mM DTT. Before use, the SPD-5 stock
1048 solution was centrifuged for 5 min at 80,000 rpm to remove residual aggregates. 5 min
1049 after formation, SPD-5 condensates were placed in glass-bottom 96-well dishes (Corning,
1050 4850, high content imaging dish) pre-cleaned with 2% Hellmanex and washed in water.
1051 For each sample, half was placed in the well undisturbed (control), and the other half was
1052 diluted 10-fold, pipetted 5 times, then placed in a well (induced disassembly). 96-well
1053 plates were imaged on an inverted Nikon Ti-E microscope using a 60x NA 1.4 Plan
1054 Apochromat oil objective, a Zyla cMOS camera (Andor), and MicroManager control
1055 software. For each image, SPD-5 condensates were identified through applying a
1056 threshold then using the particle analyzer function in FIJI. When analyzing condensate
1057 formation, we report the sum of the integrated intensities of each condensate per image
1058 (total condensate mass). Survival % plotted in Figure 5 assumes a 10-fold loss in total
1059 condensate mass due to dilution.

1060

1061 **Quantification and statistical analysis**

1062 Images were analyzed with FIJI (<https://fiji.sc/>), R (<https://www.r-project.org/>), and
1063 GraphPad Prism (<https://www.graphpad.com>). For FLUCS experiments, centrosome
1064 deformation was calculated by measuring the long axis (orthogonal to the flow direction)
1065 of PCM-localized SPD-5 at the initial and final time points of PCM deformation, prior to

1066 fracture (defined below). The deformation rate equaled the difference in PCM lengths
1067 divided by the time interval. Centrosome fracture was measured using line scans across
1068 the long axis of PCM-localized SPD-5. Fracture was scored if signal dropped to
1069 cytoplasmic levels over three consecutive pixels on the long axis across the entire flow
1070 path, and if this signal gap persisted for the rest of the images. For all other experiments,
1071 centrosome tracking and measurement was conducted using max intensity projections,
1072 correction for photobleaching, followed by thresholding and particle analysis. Thresholds
1073 were determined using: mean background intensity of the cytoplasm + b*(standard
1074 deviation of background), where b represents an integer value that is identical for all
1075 samples within an experiment. The integrated fluorescence density for the centrosome-
1076 localized signals were normalized to either the first intensity value or max intensity value
1077 (Figure 3) and plotted over time.

1078
1079 All data are expressed as the mean \pm 95% confidence intervals as stated in the figure
1080 legends and results. The value of n and what n represents (e.g., number of images,
1081 condensates or experimental replicates) is stated in figure legends and results. Normality
1082 tests were first performed before applying statistical tests. Statistical tests were
1083 performed with GraphPad Prism.

1084
1085 **REFERENCES**

1086 Begasse, M.L., M. Leaver, F. Vazquez, S.W. Grill, and A.A. Hyman. 2015. Temperature
1087 Dependence of Cell Division Timing Accounts for a Shift in the Thermal Limits of *C.*
1088 *elegans* and *C. briggsae*. *Cell Rep.* 10:647-653.

1089 Cabral, G., T. Laos, J. Dumont, and A. Dammermann. 2019. Differential Requirements for
1090 Centrioles in Mitotic Centrosome Growth and Maintenance. *Dev Cell.* 50:355-366 e356.

1091 Carvalho, A., S.K. Olson, E. Gutierrez, K. Zhang, L.B. Noble, E. Zanin, A. Desai, A. Groisman, and
1092 K. Oegema. 2011. Acute drug treatment in the early *C. elegans* embryo. *PLoS One.*
1093 6:e24656.

1094 Colombo, K., S.W. Grill, R.J. Kimple, F.S. Willard, D.P. Siderovski, and P. Gonczy. 2003.
1095 Translation of polarity cues into asymmetric spindle positioning in *Caenorhabditis*
1096 *elegans* embryos. *Science.* 300:1957-1961.

1097 Conduit, P.T., K. Brunk, J. Dobbelaere, C.I. Dix, E.P. Lucas, and J.W. Raff. 2010. Centrioles
1098 regulate centrosome size by controlling the rate of Cnn incorporation into the PCM.
1099 *Current biology : CB.* 20:2178-2186.

1100 Conduit, P.T., Z. Feng, J.H. Richens, J. Baumbach, A. Wainman, S.D. Bakshi, J. Dobbelaere, S.
1101 Johnson, S.M. Lea, and J.W. Raff. 2014a. The centrosome-specific phosphorylation of
1102 Cnn by Polo/Plk1 drives Cnn scaffold assembly and centrosome maturation. *Dev Cell*.
1103 28:659-669.

1104 Conduit, P.T., J.H. Richens, A. Wainman, J. Holder, C.C. Vicente, M.B. Pratt, C.I. Dix, Z.A. Novak,
1105 I.M. Dobbie, L. Schermelleh, and J.W. Raff. 2014b. A molecular mechanism of mitotic
1106 centrosome assembly in *Drosophila*. *eLife*. 3:e03399.

1107 Conduit, P.T., A. Wainman, and J.W. Raff. 2015. Centrosome function and assembly in animal
1108 cells. *Nature reviews. Molecular cell biology*. 16:611-624.

1109 Decker, M., S. Jaensch, A. Pozniakovsky, A. Zinke, K.F. O'Connell, W. Zachariae, E. Myers, and
1110 A.A. Hyman. 2011. Limiting amounts of centrosome material set centrosome size in *C.*
1111 *elegans* embryos. *Current biology : CB*. 21:1259-1267.

1112 Doxsey, S.J., P. Stein, L. Evans, P.D. Calarco, and M. Kirschner. 1994. Pericentrin, a highly
1113 conserved centrosome protein involved in microtubule organization. *Cell*. 76:639-650.

1114 Enos, S.J., M. Dressler, B.F. Gomes, A.A. Hyman, and J.B. Woodruff. 2018. Phosphatase PP2A
1115 and microtubule-mediated pulling forces disassemble centrosomes during mitotic exit.
1116 *Biol Open*. 7.

1117 Erpf, A.C., L. Stenzel, N. Memar, M. Antoniolli, M. Osepashvili, R. Schnabel, B. Conradt, and T.
1118 Mikeladze-Dvali. 2019. PCMD-1 Organizes Centrosome Matrix Assembly in *C. elegans*.
1119 *Current biology : CB*. 29:1324-1336 e1326.

1120 Fong, K.W., Y.K. Choi, J.B. Rattner, and R.Z. Qi. 2008. CDK5RAP2 is a pericentriolar protein that
1121 functions in centrosomal attachment of the gamma-tubulin ring complex. *Mol Biol Cell*.
1122 19:115-125.

1123 Frokjaer-Jensen, C., M.W. Davis, C.E. Hopkins, B.J. Newman, J.M. Thummel, S.P. Olesen, M.
1124 Grunnet, and E.M. Jorgensen. 2008. Single-copy insertion of transgenes in
1125 *Caenorhabditis elegans*. *Nat Genet*. 40:1375-1383.

1126 George, E.P., D. Raabe, and R.O. Ritchie. 2019. High-entropy alloys. *Nature Reviews Materials*.
1127 Gomez-Ferreria, M.A., U. Rath, D.W. Buster, S.K. Chanda, J.S. Caldwell, D.R. Rines, and D.J.
1128 Sharp. 2007. Human Cep192 is required for mitotic centrosome and spindle assembly.
1129 *Current biology : CB*. 17:1960-1966.

1130 Gonczy, P., S. Grill, E.H. Stelzer, M. Kirkham, and A.A. Hyman. 2001. Spindle positioning during
1131 the asymmetric first cell division of *Caenorhabditis elegans* embryos. *Novartis Found
1132 Symp*. 237:164-175; discussion 176-181.

1133 Grill, S.W., P. Gonczy, E.H. Stelzer, and A.A. Hyman. 2001. Polarity controls forces governing
1134 asymmetric spindle positioning in the *Caenorhabditis elegans* embryo. *Nature*. 409:630-
1135 633.

1136 Grill, S.W., J. Howard, E. Schaffer, E.H. Stelzer, and A.A. Hyman. 2003. The distribution of active
1137 force generators controls mitotic spindle position. *Science*. 301:518-521.

1138 Hamill, D.R., A.F. Severson, J.C. Carter, and B. Bowerman. 2002. Centrosome maturation and
1139 mitotic spindle assembly in *C. elegans* require SPD-5, a protein with multiple coiled-coil
1140 domains. *Dev Cell*. 3:673-684.

1141 Hannak, E., M. Kirkham, A.A. Hyman, and K. Oegema. 2001. Aurora-A kinase is required for
1142 centrosome maturation in *Caenorhabditis elegans*. *J Cell Biol*. 155:1109-1116.

1143 Harashima, H., N. Dissmeyer, and A. Schnittger. 2013. Cell cycle control across the eukaryotic
1144 kingdom. *Trends Cell Biol.* 23:345-356.

1145 Haren, L., T. Stearns, and J. Luders. 2009. Plk1-dependent recruitment of gamma-tubulin
1146 complexes to mitotic centrosomes involves multiple PCM components. *PLoS One.*
1147 4:e5976.

1148 Joukov, V., J.C. Walter, and A. De Nicolo. 2014. The Cep192-organized aurora A-Plk1 cascade is
1149 essential for centrosome cycle and bipolar spindle assembly. *Mol Cell.* 55:578-591.

1150 Kemp, C.A., K.R. Kopish, P. Zipperlen, J. Ahringer, and K.F. O'Connell. 2004. Centrosome
1151 maturation and duplication in *C. elegans* require the coiled-coil protein SPD-2. *Dev Cell.*
1152 6:511-523.

1153 Labbe, J.C., E.K. McCarthy, and B. Goldstein. 2004. The forces that position a mitotic spindle
1154 asymmetrically are tethered until after the time of spindle assembly. *J Cell Biol.* 167:245-
1155 256.

1156 Laos, T., G. Cabral, and A. Dammermann. 2015. Isotropic incorporation of SPD-5 underlies
1157 centrosome assembly in *C. elegans*. *Current biology : CB.* 25:R648-649.

1158 Lee, K., and K. Rhee. 2011. PLK1 phosphorylation of pericentrin initiates centrosome maturation
1159 at the onset of mitosis. *J Cell Biol.* 195:1093-1101.

1160 Lemaitre, R.P., A. Bogdanova, B. Borgonovo, J.B. Woodruff, and D.N. Drechsel. 2019. FlexiBAC: a
1161 versatile, open-source baculovirus vector system for protein expression, secretion, and
1162 proteolytic processing. *BMC Biotechnol.* 19:20.

1163 Lindon, C., and J. Pines. 2004. Ordered proteolysis in anaphase inactivates Plk1 to contribute to
1164 proper mitotic exit in human cells. *J Cell Biol.* 164:233-241.

1165 Magescas, J., J.C. Zonka, and J.L. Feldman. 2019. A two-step mechanism for the inactivation of
1166 microtubule organizing center function at the centrosome. *eLife.* 8.

1167 McNally, F.J. 2013. Mechanisms of spindle positioning. *J Cell Biol.* 200:131-140.

1168 Megraw, T.L., S. Kilaru, F.R. Turner, and T.C. Kaufman. 2002. The centrosome is a dynamic
1169 structure that ejects PCM flares. *J Cell Sci.* 115:4707-4718.

1170 Mittasch, M., P. Gross, M. Nestler, A.W. Fritsch, C. Iserman, M. Kar, M. Munder, A. Voigt, S.
1171 Alberti, S.W. Grill, and M. Kreysing. 2018. Non-invasive perturbations of intracellular
1172 flow reveal physical principles of cell organization. *Nat Cell Biol.* 20:344-351.

1173 Nguyen-Ngoc, T., K. Afshar, and P. Gonczy. 2007. Coupling of cortical dynein and G alpha
1174 proteins mediates spindle positioning in *Caenorhabditis elegans*. *Nat Cell Biol.* 9:1294-
1175 1302.

1176 Ozlu, N., M. Srayko, K. Kinoshita, B. Habermann, T. O'Toole E, T. Muller-Reichert, N. Schmalz, A.
1177 Desai, and A.A. Hyman. 2005. An essential function of the *C. elegans* ortholog of TPX2 is
1178 to localize activated aurora A kinase to mitotic spindles. *Dev Cell.* 9:237-248.

1179 Paix, A., A. Folkmann, D. Rasoloson, and G. Seydoux. 2015. High Efficiency, Homology-Directed
1180 Genome Editing in *Caenorhabditis elegans* Using CRISPR-Cas9 Ribonucleoprotein
1181 Complexes. *Genetics.* 201:47-54.

1182 Paix, A., A. Folkmann, and G. Seydoux. 2017. Precision genome editing using CRISPR-Cas9 and
1183 linear repair templates in *C. elegans*. *Methods.* 121-122:86-93.

1184 Panbianco, C., D. Weinkove, E. Zanin, D. Jones, N. Divecha, M. Gotta, and J. Ahringer. 2008. A
1185 casein kinase 1 and PAR proteins regulate asymmetry of a PIP(2) synthesis enzyme for
1186 asymmetric spindle positioning. *Dev Cell.* 15:198-208.

1187 Pecreaux, J., J.C. Roper, K. Kruse, F. Julicher, A.A. Hyman, S.W. Grill, and J. Howard. 2006.
1188 Spindle oscillations during asymmetric cell division require a threshold number of active
1189 cortical force generators. *Current biology : CB*. 16:2111-2122.

1190 Pelletier, L., N. Ozlu, E. Hannak, C. Cowan, B. Habermann, M. Ruer, T. Muller-Reichert, and A.A.
1191 Hyman. 2004. The *Caenorhabditis elegans* centrosomal protein SPD-2 is required for
1192 both pericentriolar material recruitment and centriole duplication. *Current biology : CB*.
1193 14:863-873.

1194 Pimenta-Marques, A., I. Bento, C.A. Lopes, P. Duarte, S.C. Jana, and M. Bettencourt-Dias. 2016.
1195 A mechanism for the elimination of the female gamete centrosome in *Drosophila*
1196 *melanogaster*. *Science*. 353:aaf4866.

1197 Rual, J.F., J. Ceron, J. Koreth, T. Hao, A.S. Nicot, T. Hirozane-Kishikawa, J. Vandenhoute, S.H.
1198 Orkin, D.E. Hill, S. van den Heuvel, and M. Vidal. 2004. Toward improving *Caenorhabditis*
1199 *elegans* phenome mapping with an ORFeome-based RNAi library. *Genome Res*. 14:2162-
1200 2168.

1201 Schlaitz, A.L., M. Srayko, A. Dammermann, S. Quintin, N. Wielsch, I. MacLeod, Q. de Robillard, A.
1202 Zinke, J.R. Yates, 3rd, T. Muller-Reichert, A. Shevchenko, K. Oegema, and A.A. Hyman.
1203 2007. The *C. elegans* RSA complex localizes protein phosphatase 2A to centrosomes and
1204 regulates mitotic spindle assembly. *Cell*. 128:115-127.

1205 Severson, A.F., and B. Bowerman. 2003. Myosin and the PAR proteins polarize microfilament-
1206 dependent forces that shape and position mitotic spindles in *Caenorhabditis elegans*. *J
1207 Cell Biol*. 161:21-26.

1208 Sun, T.L., T. Kurokawa, S. Kuroda, A.B. Ihsan, T. Akasaki, K. Sato, M.A. Haque, T. Nakajima, and
1209 J.P. Gong. 2013. Physical hydrogels composed of polyampholytes demonstrate high
1210 toughness and viscoelasticity. *Nat Mater*. 12:932-937.

1211 Sunkel, C.E., and D.M. Glover. 1988. polo, a mitotic mutant of *Drosophila* displaying abnormal
1212 spindle poles. *J Cell Sci*. 89 (Pt 1):25-38.

1213 Weinert, F.M., J.A. Kraus, T. Franosch, and D. Braun. 2008. Microscale fluid flow induced by
1214 thermoviscous expansion along a traveling wave. *Phys Rev Lett*. 100:164501.

1215 Wlodarchak, N., and Y. Xing. 2016. PP2A as a master regulator of the cell cycle. *Crit Rev Biochem
1216 Mol Biol*. 51:162-184.

1217 Woodruff, J.B., B. Ferreira Gomes, P.O. Widlund, J. Mahamid, A. Honigmann, and A.A. Hyman.
1218 2017. The Centrosome Is a Selective Condensate that Nucleates Microtubules by
1219 Concentrating Tubulin. *Cell*. 169:1066-1077 e1010.

1220 Woodruff, J.B., and A.A. Hyman. 2015. Method: In vitro analysis of pericentriolar material
1221 assembly. *Methods Cell Biol*. 129:369-382.

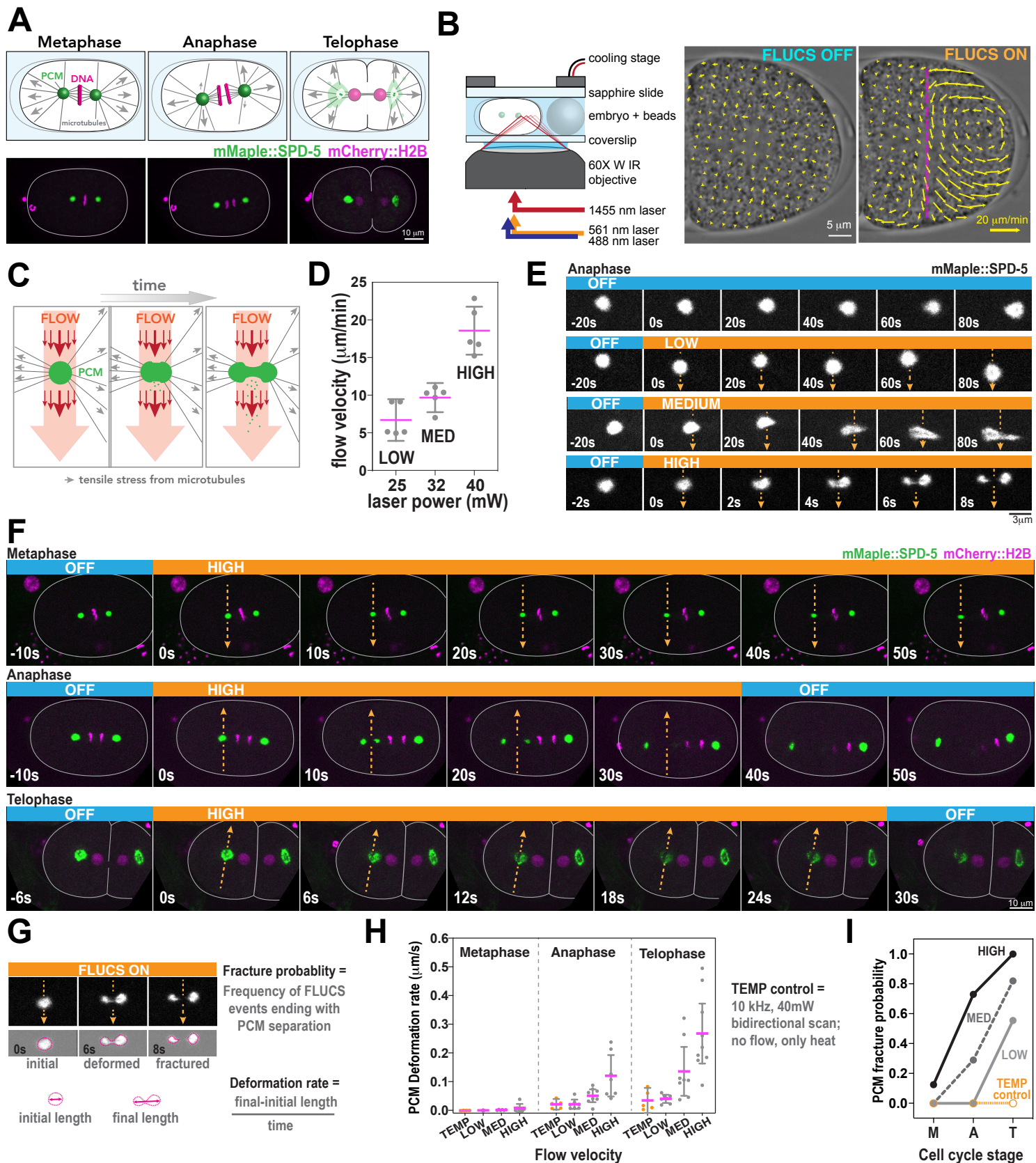
1222 Woodruff, J.B., O. Wueseke, and A.A. Hyman. 2014. Pericentriolar material structure and
1223 dynamics. *Philos Trans R Soc Lond B Biol Sci*. 369.

1224 Woodruff, J.B., O. Wueseke, V. Viscardi, J. Mahamid, S.D. Ochoa, J. Bunkenborg, P.O. Widlund,
1225 A. Pozniakovsky, E. Zanin, S. Bahmanyar, A. Zinke, S.H. Hong, M. Decker, W. Baumeister,
1226 J.S. Andersen, K. Oegema, and A.A. Hyman. 2015. Centrosomes. Regulated assembly of a
1227 supramolecular centrosome scaffold in vitro. *Science*. 348:808-812.

1228 Zebrowski, D.C., S. Vergarajauregui, C.C. Wu, T. Piatkowski, R. Becker, M. Leone, S. Hirth, F.
1229 Ricciardi, N. Falk, A. Giessl, S. Just, T. Braun, G. Weidinger, and F.B. Engel. 2015.

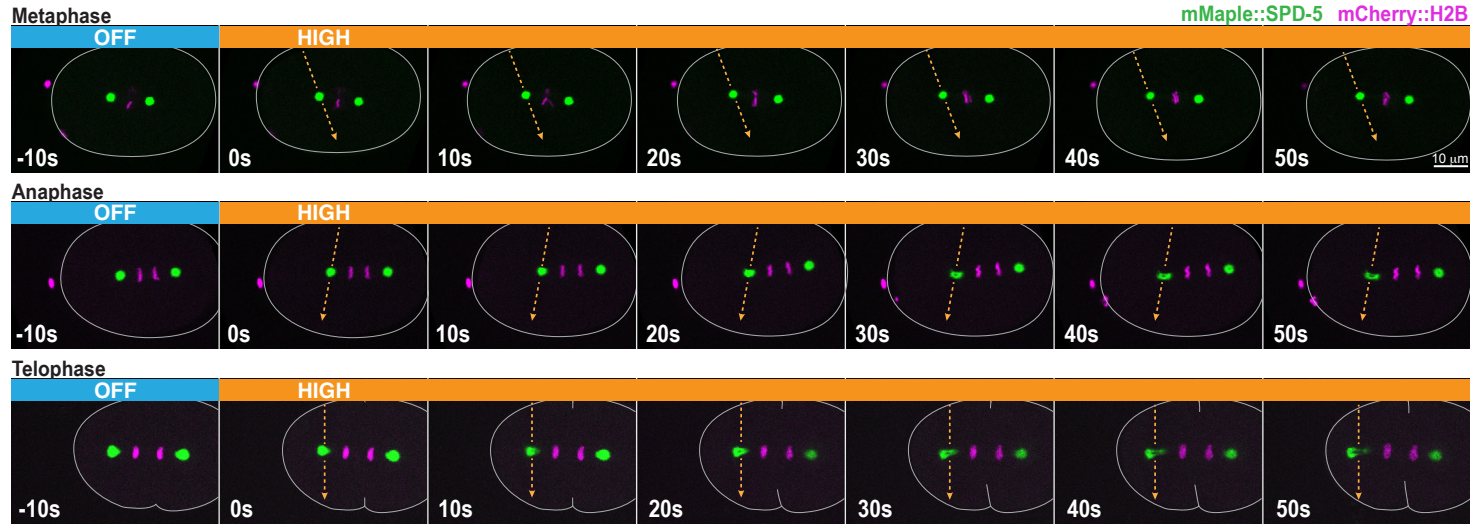
1230 Developmental alterations in centrosome integrity contribute to the post-mitotic state
1231 of mammalian cardiomyocytes. *eLife*. 4.
1232 Zhu, F., S. Lawo, A. Bird, D. Pinchev, A. Ralph, C. Richter, T. Muller-Reichert, R. Kittler, A.A.
1233 Hyman, and L. Pelletier. 2008. The mammalian SPD-2 ortholog Cep192 regulates
1234 centrosome biogenesis. *Current biology : CB*. 18:136-141.
1235

Mittasch et al. Figure 1

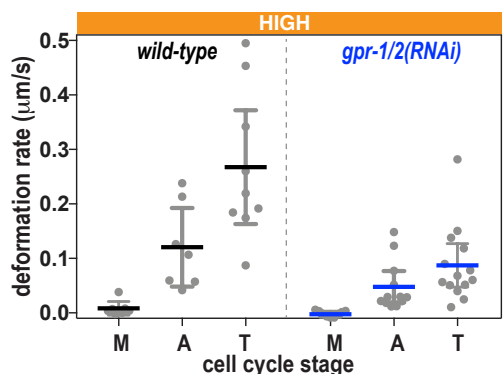


Mittasch et al. Figure 2

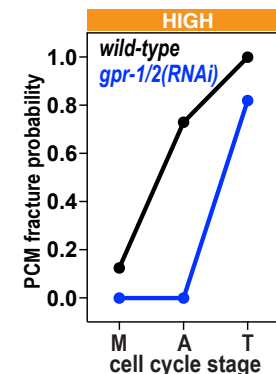
A *gpr-1/2(RNAi)* -- reduced cortical pulling force



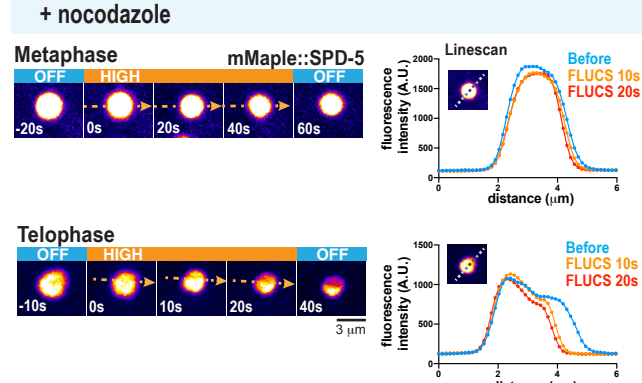
B



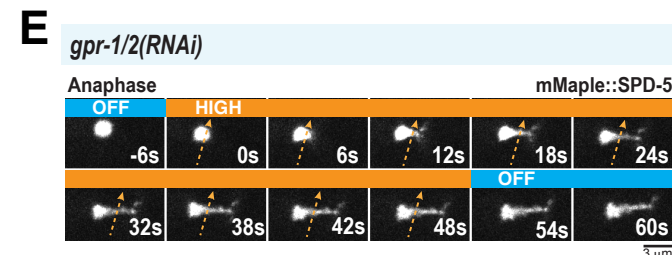
C



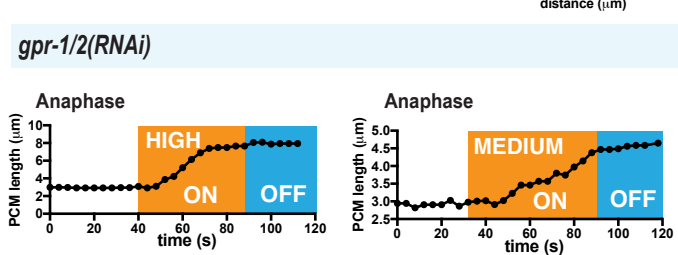
D



E

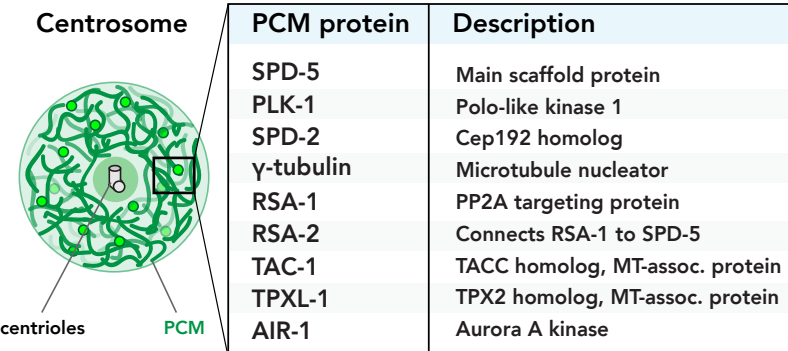


F

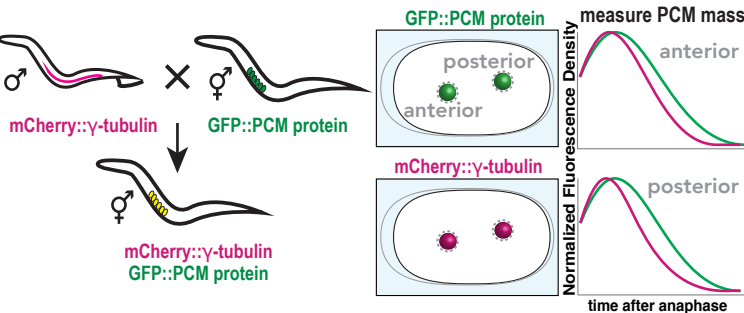


Mittasch et al. Figure 3

A

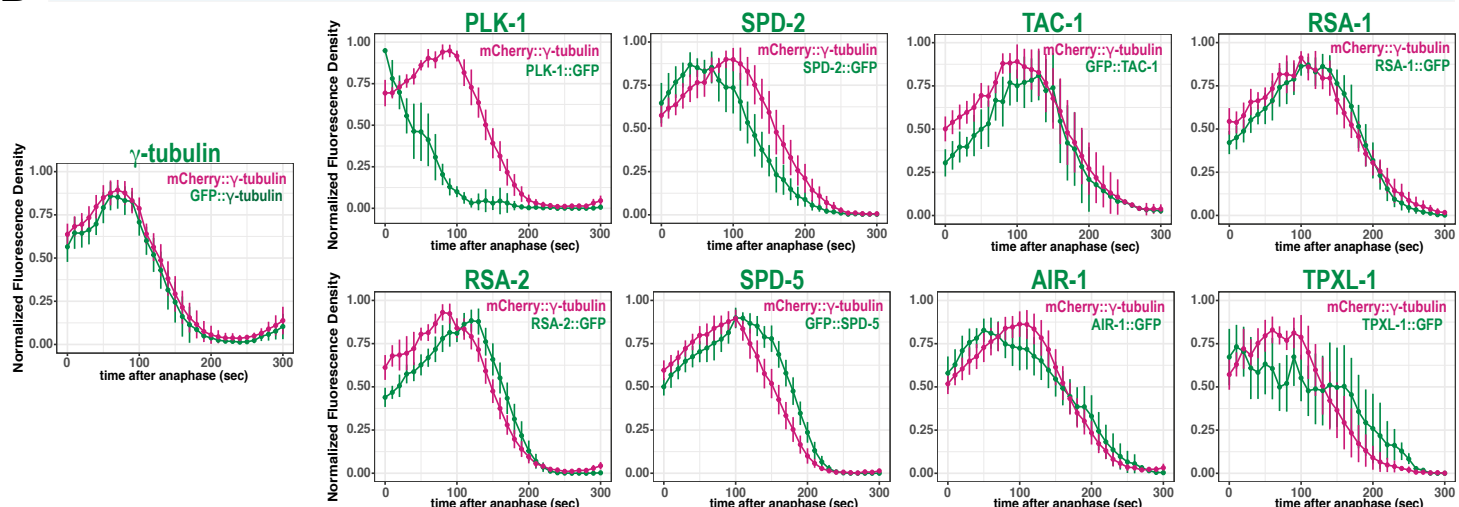


B



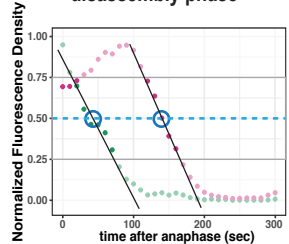
D

Disassembly profiles for anterior PCM proteins

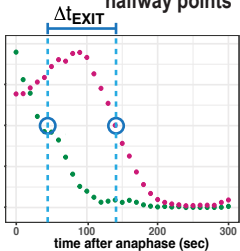


E

1. fit linear part of disassembly phase

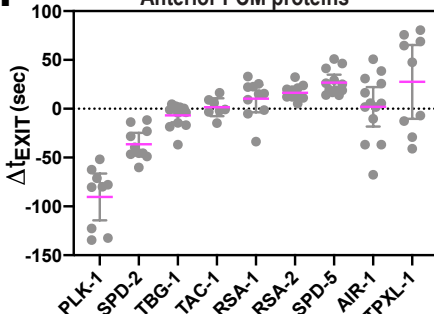


2. calculate time between halfway points



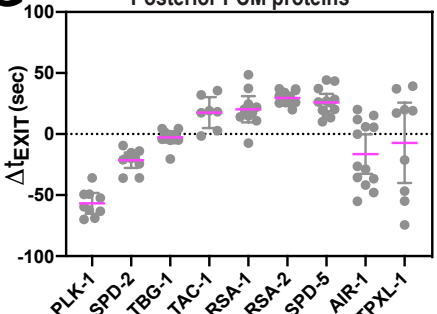
F

Anterior PCM proteins

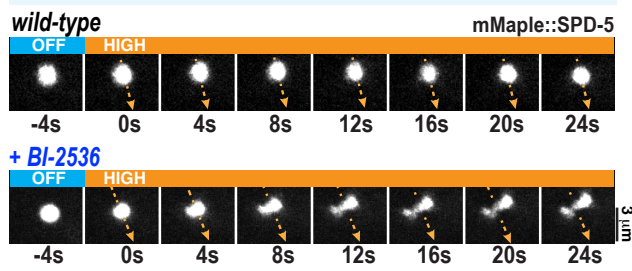


G

Posterior PCM proteins

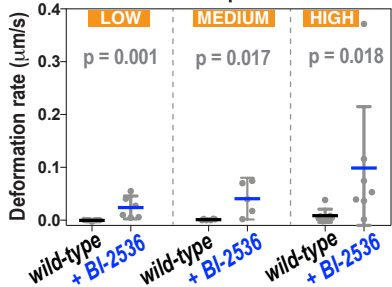


A Inhibition of PLK-1 in Metaphase



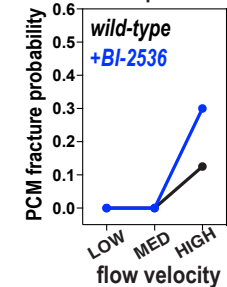
B

Metaphase

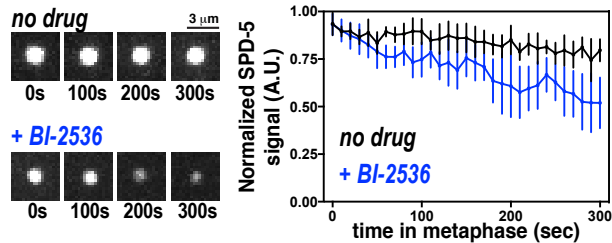


C

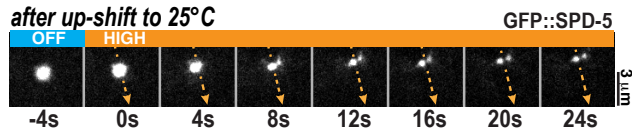
Metaphase



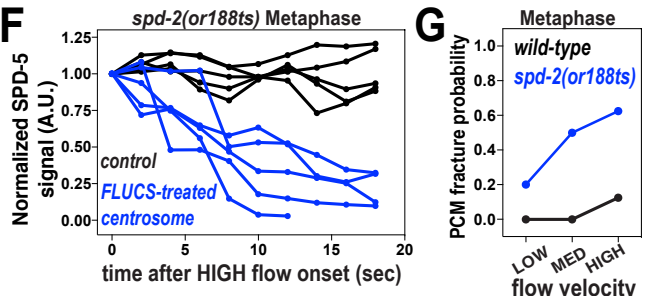
D PCM stability in Metaphase-arrested embryos



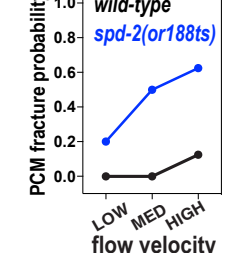
E *spd-2(or188ts)* in Metaphase



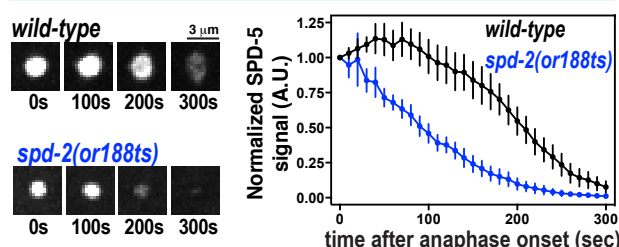
F *spd-2(or188ts)* Metaphase



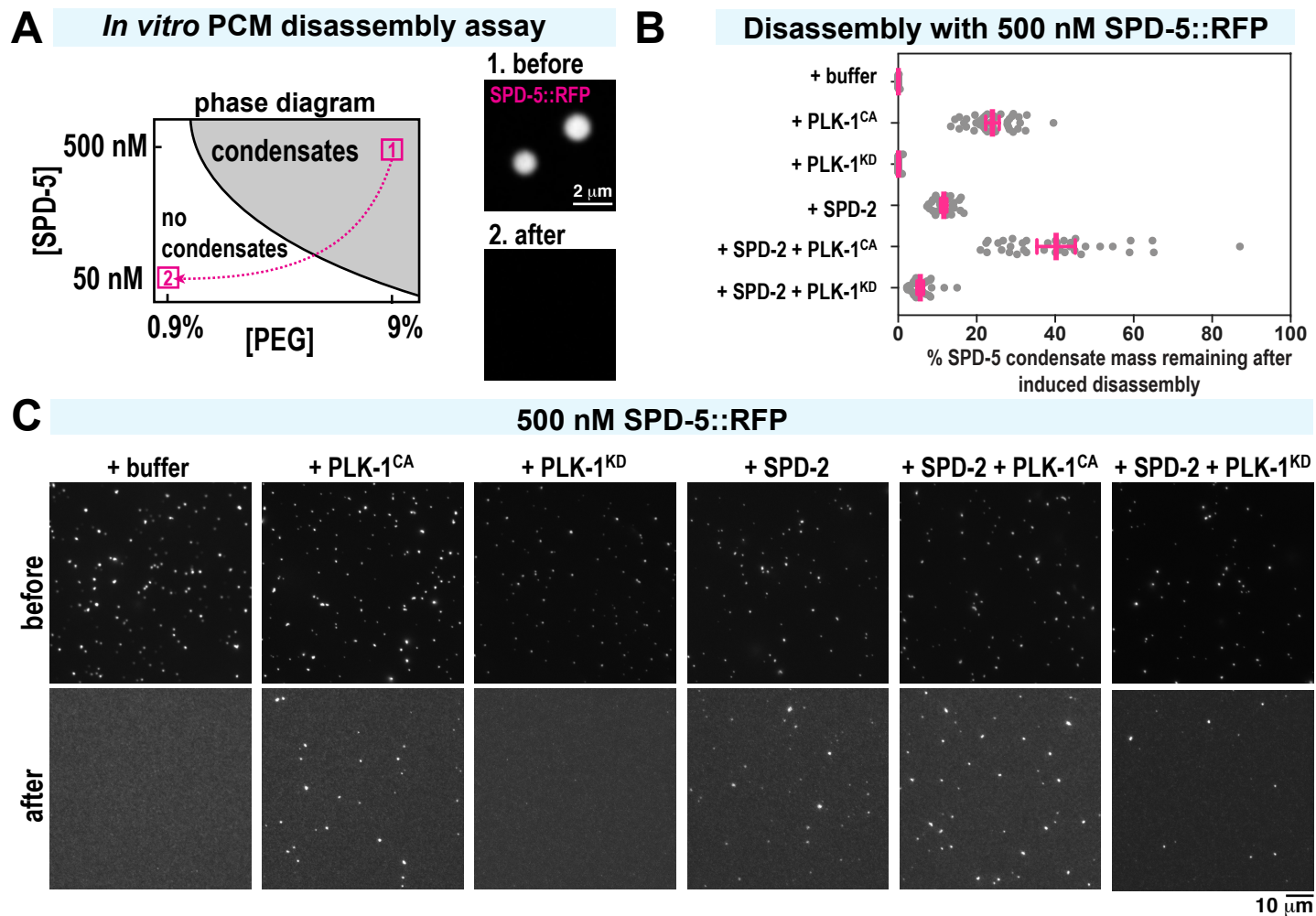
G Metaphase

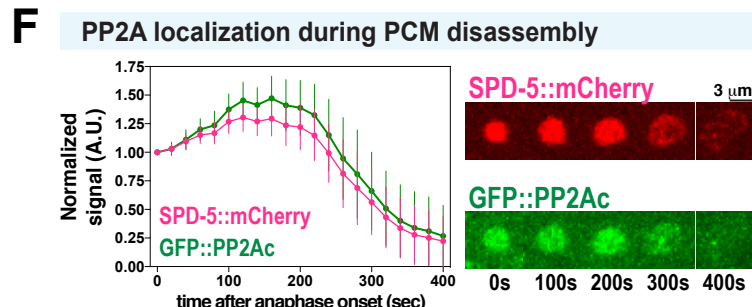
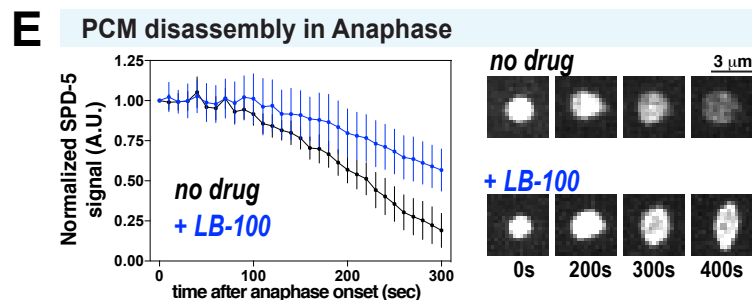
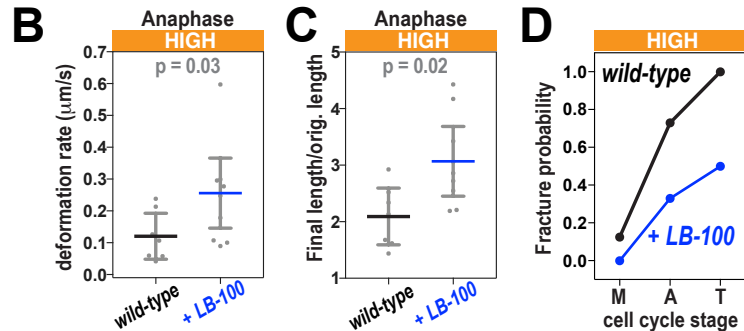
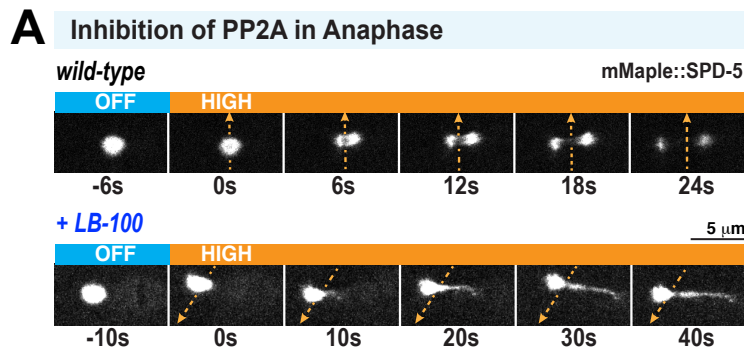


H PCM disassembly in Anaphase

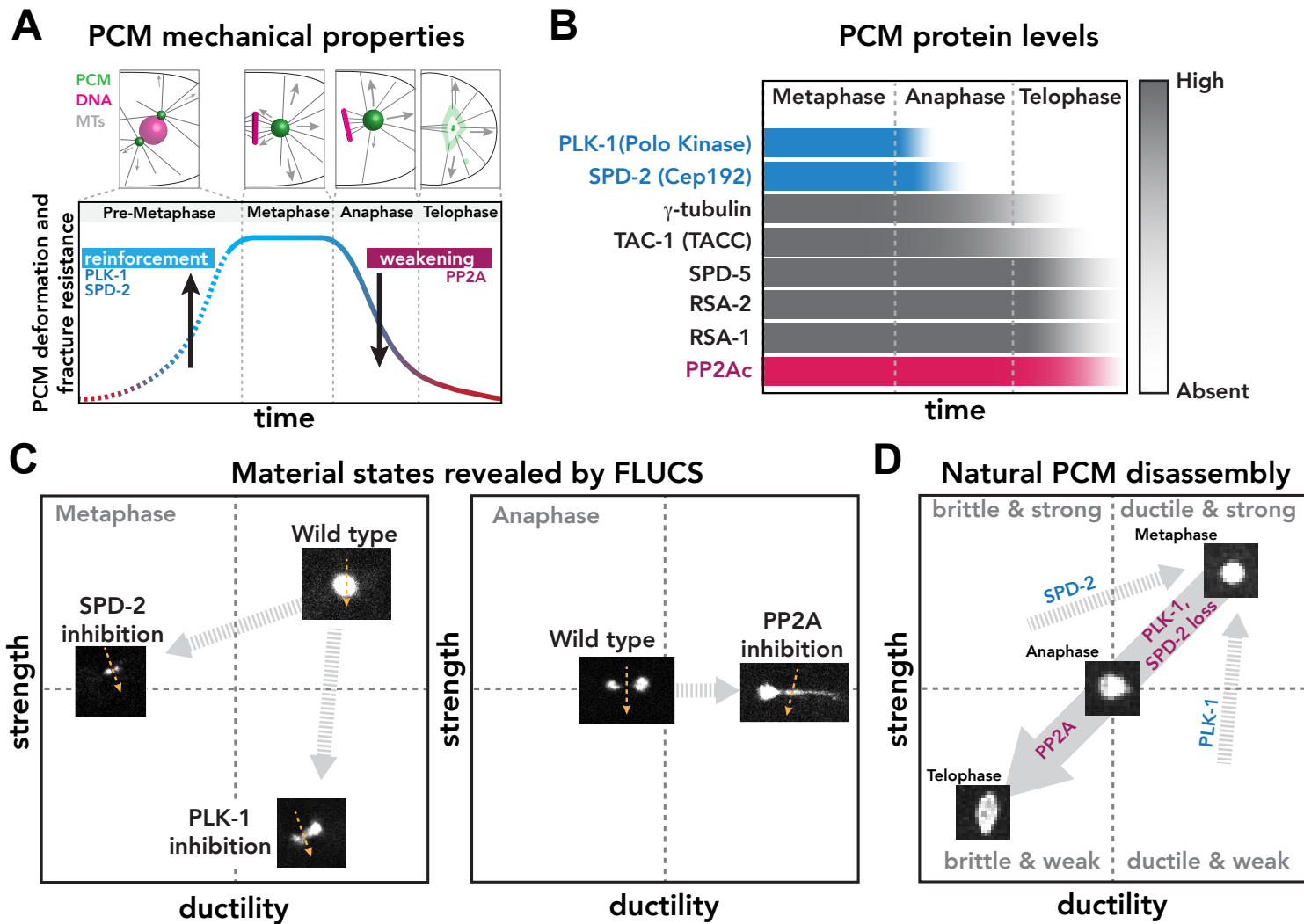


Mittasch et al. Figure 5

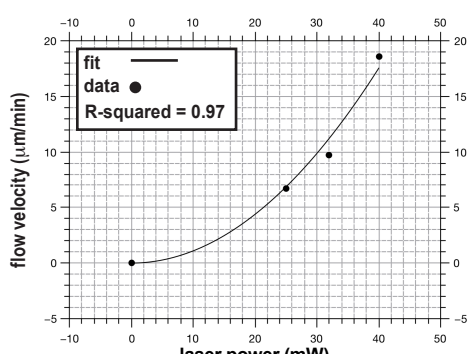




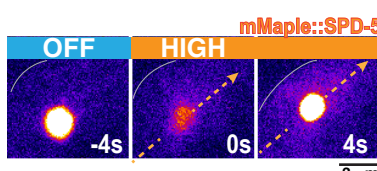
Mittasch et al. Figure 7



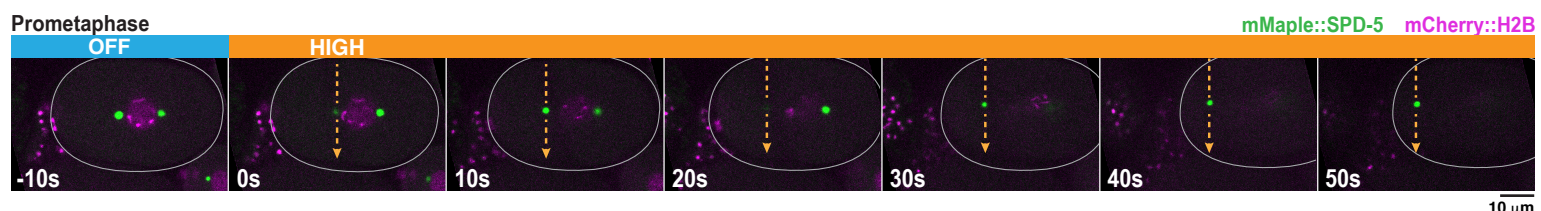
A



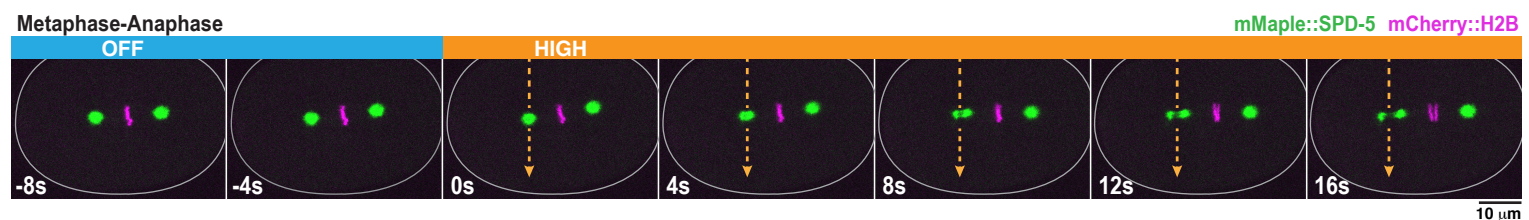
B



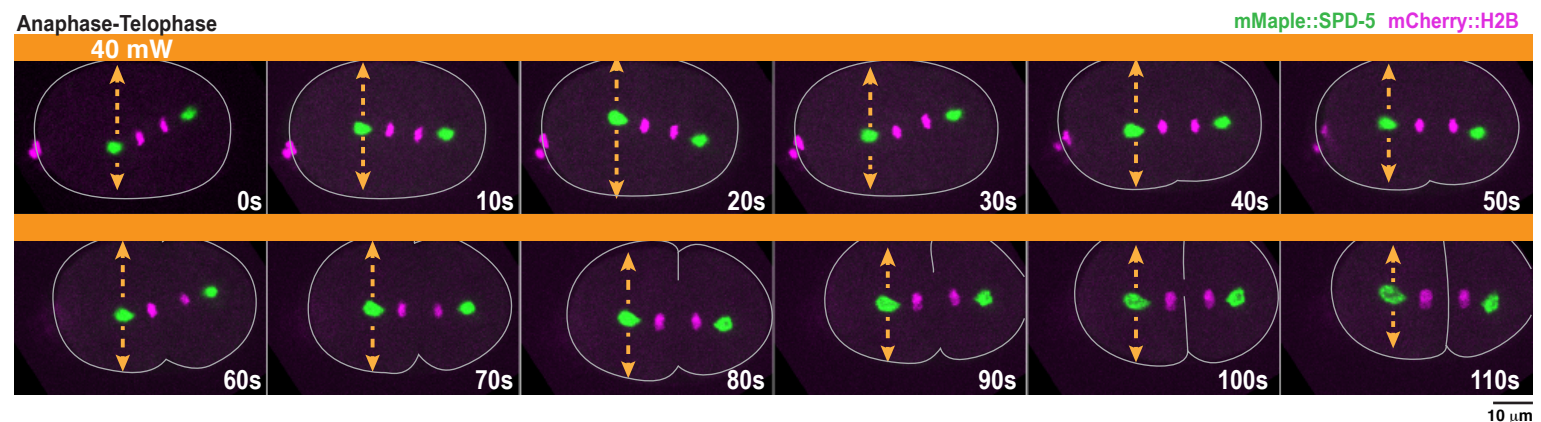
C



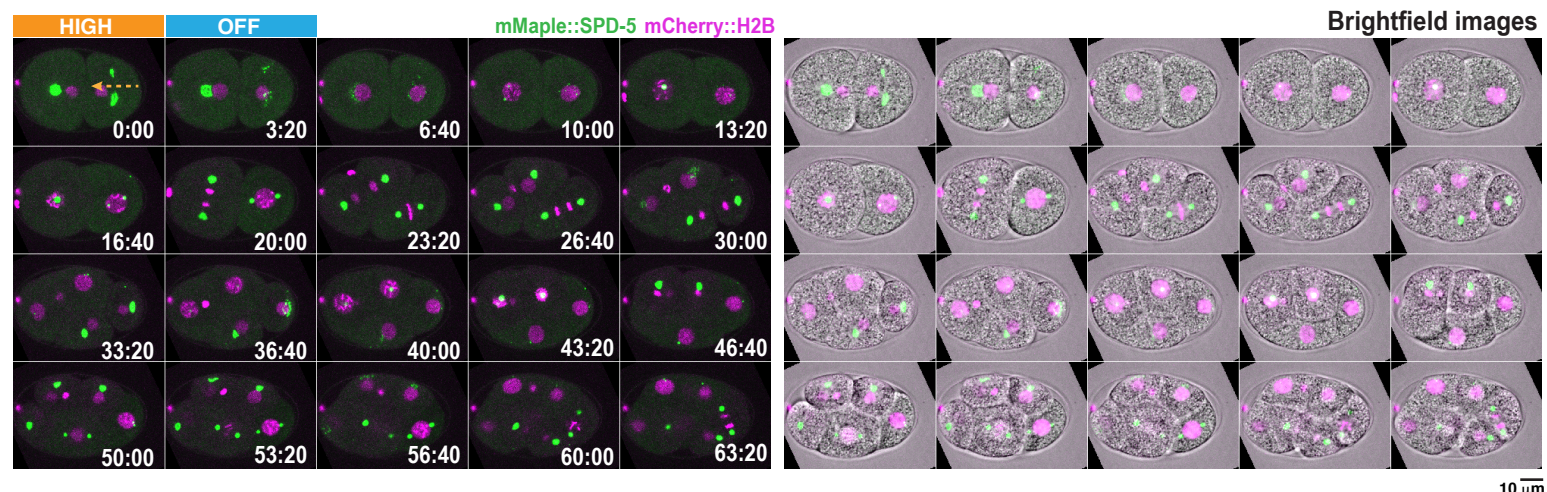
D Continuous FLUCS during metaphase-anaphase transition



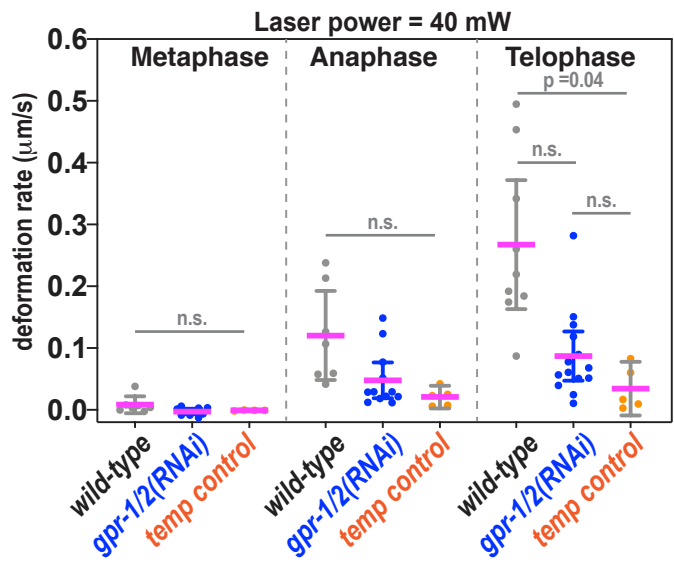
E 10 kHz, bidirectional laser scan---no flow, only heat



F Embryo survival after FLUCS in one-cell stage

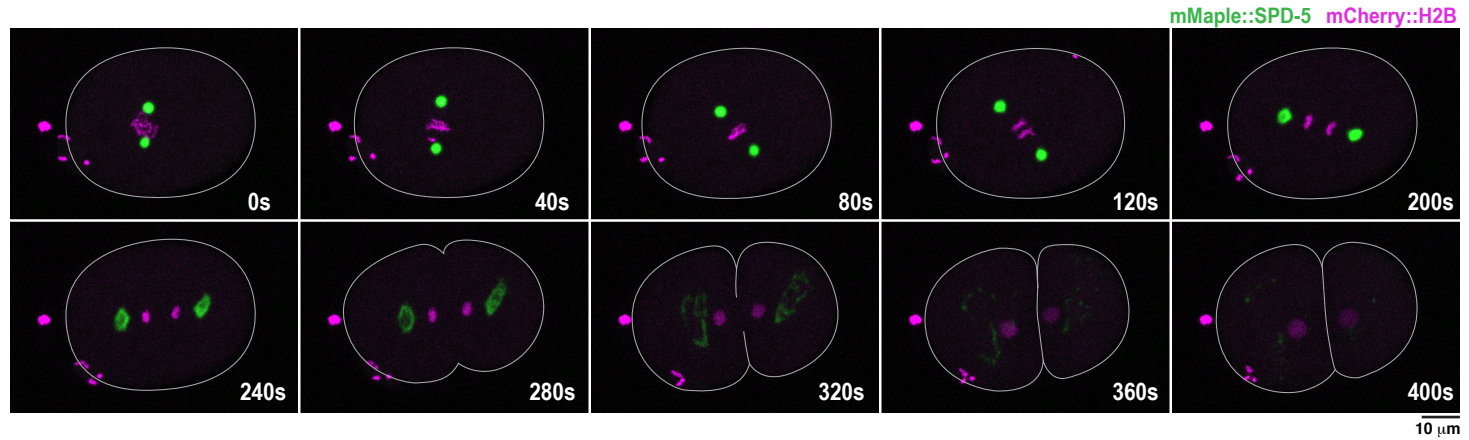


A



B

csnk-1RNAi) --- increased pulling forces throughout the cell cycle



Disassembly profiles for posterior PCM proteins

